

Massive and refined: a sample of large galaxy clusters simulated at high resolution. I: Thermal gas and properties of shock waves.

F. Vazza[1,3]; G. Brunetti[1]; C. Gheller[2]; R. Brunino[2]

^aINAF/Istituto di Radioastronomia, via Gobetti 101, I-40129 Bologna, Italy

^bCINECA, High Performance System Division, Casalecchio di Reno–Bologna, Italy

^cvazza@ira.inaf.it

Abstract

We present a sample of 20 massive galaxy clusters with total virial masses in the range of $6 \cdot 10^{14} M_{\odot} \leq M_{vir} \leq 2 \cdot 10^{15} M_{\odot}$, re-simulated with a customized version of the 1.5. ENZO code employing Adaptive Mesh Refinement. This technique allowed us to obtain unprecedented high spatial resolution ($\approx 25 kpc/h$) up to the distance of ~ 3 virial radii from the clusters center, and makes it possible to focus with the same level of detail on the physical properties of the innermost and of the outermost cluster regions, providing new clues on the role of shock waves and turbulent motions in the ICM, across a wide range of scales.

In this paper, a first exploratory study of this data set is presented. We report on the thermal properties of galaxy clusters at $z = 0$. Integrated and morphological properties of gas density, gas temperature, gas entropy and baryon fraction distributions are discussed, and compared with existing outcomes both from the observational and from the numerical literature. Our cluster sample shows an overall good consistency with the results obtained adopting other numerical techniques (e.g. Smoothed Particles Hydrodynamics), yet it provides a more accurate representation of the accretion patterns far outside the cluster cores. We also reconstruct the properties of shock waves within the sample by means of a velocity-based approach, and we study Mach numbers and energy distributions for the various dynamical states in clusters, giving estimates for the injection of Cosmic Rays particles at shocks. The present sample is rather unique in the panorama of cosmological simulations of massive galaxy clusters, due to its dynamical range, statistics of objects and number of time outputs. For this reason, we deploy a public repository of the available data, accessible via web portal at <http://data.cineca.it>.

Key words: Galaxies:clusters, large-scale structure of universe, methods: numerical, shock waves, hydrodynamics

1. Introduction

Simulating the evolution of Cosmological Large Scale Structures of the Universe is a challenging task. In the last thirty years different numerical techniques were designed to follow the dynamics of the most important matter/energy components of the Universe: Dark Matter (DM), baryonic matter, and dark energy. In order to account for the great complexity and for the number of details provided by real cluster observations, a number of physical processes in addition to gravitational col-

lapse and non-radiative hydro-dynamics have been implemented in many numerical works in the last few years: radiative gas processes, magnetic fields, star formations, AGN feedback, Cosmic Rays, turbulence, etc. (e.g. Dolag et al. 2008; Borgani & Kravtsov 2009, and references therein, for a recent review).

At present, two main numerical approaches are massively applied to cosmological numerical simulations: Lagrangian methods, which sample both the DM and the gas properties using point-like fluid elements, usually regarded as particles (e.g. Smoothed Particles Hydrody-

namics codes, SPH) and Eulerian methods, which reconstruct the gas properties with a discrete space sampling with regular or adaptive meshes and model the Dark Matter properties with a Particle Mesh approach (see Dolag et al.2008 and references therein for a modern review).

High resolution, AMR simulations (such as the ENZO simulations presented in this paper) can provide an accurate representation of the cosmic gas dynamics in galaxy clusters, achieving a very large dynamical range. Recent works have shown that the adoption of proper mesh refinement criteria allows to study also the details of chaotic motions in the ICM (e.g. Iapichino & Niemeyer 2008, Vazza et al.2009; Maier et al.2009; Vazza, Gheller & Brunetti 2010; Paul et al.2010)

Vazza et al.(2009, hereafter Va09) recently focused on the re-simulation of galaxy clusters by employing a new mesh refinement criterion, which couples the “standard” refinement criteria based on large gas or DM overdensities, to the mesh refinement criterion based on cell to cell 1–D jumps of the velocity field. In Va09 and Vazza, Gheller & Brunetti (2010, hereafter VGB10) we showed that the extra-refinement on 1–D velocity jumps opportunely increases the number of resolution elements across the ICM volume, allowing us to achieve a better spectral and morphological representation of chaotic motions in the ICM. Furthermore it reduces the artificial dampening of mixing motions due to the effect of the coarse resolution.

Since the above works were focused on the re-simulation of a few intermediate mass systems (e.g. $M < 3 \cdot 10^{14} M_{\odot}$), it is interesting now to extend the same method to a larger sample of higher mass clusters. Here we present the first results obtained analyzing 20 galaxy clusters, with total masses in the range $6 \cdot 10^{14} M_{\odot} \leq M_{vir} \leq 2 \cdot 10^{15} M_{\odot}$, obtained with the above techniques and designed to reach very high *spatial* resolution around both DM/gas clumps, shocks and turbulent motions. Such rich sample accounts for objects of very different dynamical history and it is characterized by a large dynamical range ($N_{AMR} \sim 500^3$, where N_{AMR} is the number of grid elements at the maximum mesh refinement level) within the clusters volume. This allows us to study a broad variety of multi-scale phenomena associated to cluster growth and evolution.

The paper is organized as follows: in Section 2 we

Table 1: Main characteristics of the simulated clusters at $z = 0$. Column 1: identification number; 2: total virial mass ($M_{vir} = M_{DM} + M_{gas}$); 3: virial radius (R_v); 4: $X = E_k/E_{tot}$ ratio inside R_v ; 5:dynamical classification: RE=relaxing, ME=merging or MM=major merger (with approximate redshift of the last merger event).

ID	M_{vir} [$10^{15} M_{\odot}$]	R_v [Mpc]	X [E_{kin}/E_{tot}]	note
E1	1.12	2.67	0.43	MM(0.1)
E2	1.12	2.73	0.47	ME
E3A	1.38	2.82	0.43	MM(0.2)
E3B	0.76	2.31	0.55	ME
E4	1.36	2.80	0.44	MM(0.5)
E5A	0.86	2.39	0.47	ME
E5B	0.66	2.18	0.75	ME
E7	0.65	2.19	0.45	ME
E11	1.25	2.72	0.40	MM(0.6)
E14	1.00	2.60	0.23	RE
E15A	1.01	2.63	0.85	ME
E15B	0.80	2.36	0.33	RE
E16A	1.92	3.14	0.36	RE
E16B	1.90	3.14	0.67	MM(0.2)
E18A	1.91	3.14	0.37	MM(0.8)
E18B	1.37	2.80	0.34	MM(0.5)
E18C	0.60	2.08	0.55	MM(0.3)
E21	0.68	2.18	0.40	RE
E26	0.74	2.27	0.29	MM(0.1)
E62	1.00	2.50	0.63	MM(0.9)

present the clusters sample, the numerical techniques adopted and the archiving procedure for the data sample; in Section 3.1 we present the integrated (e.g. scaling laws) properties of our clusters, in Section 3.2 we present the and radial properties of gas density, gas temperature and gas entropy for all clusters in the sample. In Section 3.3 we characterize shock waves within the clusters and give estimates on the energy level of injected Cosmic Rays particles. The discussion and the conclusions are reported in Section 4. In the Appendix, we report consistency tests for the adopted re-ionization scheme (Sect.A), and present a visual inspection of all clusters of the sample (Sect.B).

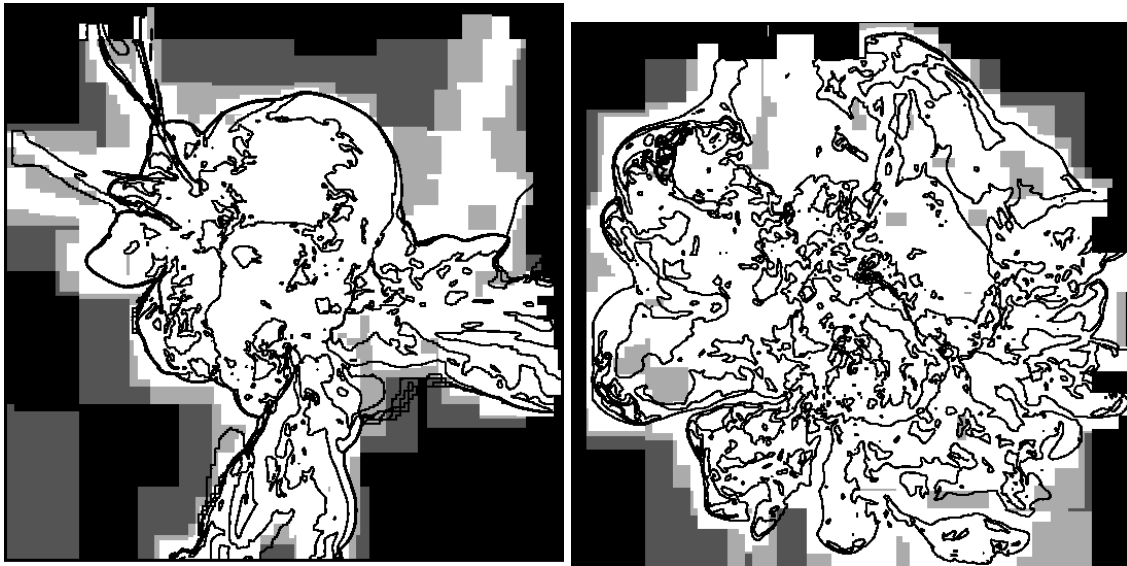


Figure 1: The hierarchy of refinement levels in our runs. Color maps: level of mesh refinement for slices through the center of cluster E1 (left panel) and E18A (right panel) at $z = 0$, from level=0 ($\Delta = 200kpc/h$, in black color) to level=3 ($\Delta = 25kpc/h$, in white color); the contour map shows the gas temperature distribution within the same region (the contours are equally spaced in $\Delta \log(T) \approx 0.5$). The side of both images is $\approx 14Mpc/h$.

2. Numerical Methods

2.1. The ENZO code

Computations presented in this work were performed using the ENZO code developed by the Laboratory for Computational Astrophysics at the University of California in San Diego (<http://lca.ucsd.edu>).

ENZO is an adaptive mesh refinement (AMR) cosmological hybrid code highly optimized for high performance computing (Bryan & Norman 1997; Norman et al.2007).

It uses a particle-mesh N-body method (PM) to follow the dynamics of the collision-less Dark Matter (DM) component (Hockney & Eastwood 1981), and an adaptive mesh method for ideal fluid-dynamics (Berger & Colella, 1989).

The DM component is coupled to the baryonic matter (gas), via gravitational forces, calculated from the total mass distribution (DM+gas) solving the Poisson equation with a FFT based approach. The gas component is described as a perfect fluid and its dynamics is calculated solving conservation equations of mass, energy and mo-

mentum over a computational mesh, using an Eulerian solver based on the Piecewise Parabolic Method (PPM, Woodward & Colella, 1984). This scheme is a higher order extension of Godunov’s shock capturing method (Godunov 1959), and it is at least second-order accurate in space outside of shocks (up to the fourth-order in 1-D, in the case of smooth flows and small time-steps) and second-order accurate in time.

2.2. Clusters simulations

For the simulations presented here, we assumed a “concordance” Λ CDM cosmology with $\Omega_0 = 1.0$, $\Omega_{BM} = 0.0441$, $\Omega_{DM} = 0.2139$, $\Omega_{\Lambda} = 0.742$, Hubble parameter $h = 0.72$ and a normalization for the primordial density power spectrum $\sigma_8 = 0.8$.

The clusters considered in this paper were extracted from a few simulations of cosmological volumes with linear size of $\approx 190Mpc/h$. For each simulation we adopted a root grid of 220^3 cells and the same number of DM particles. This leads to a DM mass resolution of $m_{dm} \approx 4.3 \cdot 10^{10}M_{\odot}/h$. The overall simulated cosmic

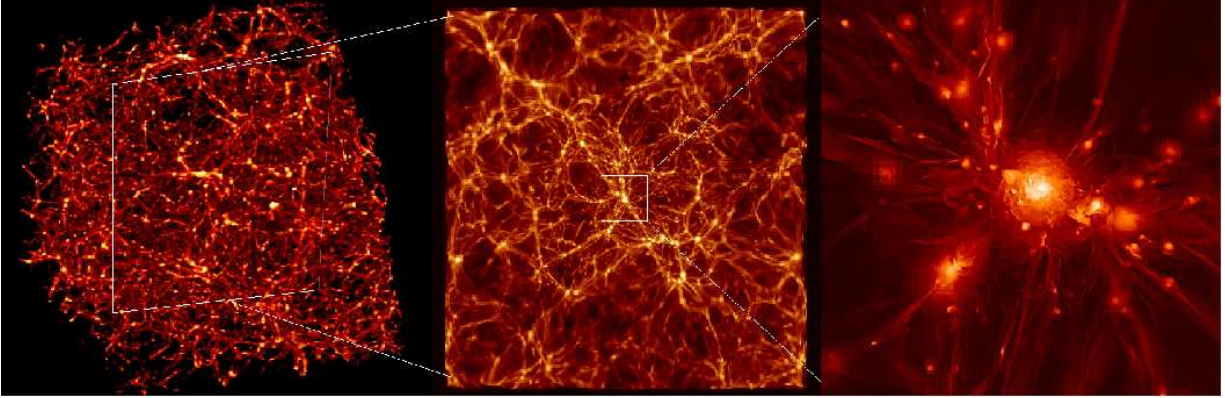


Figure 2: *Left*: 3-D rendering of gas matter within a $187Mpc/h$ computational box at $z = 0$. *Center*: slice of thickness $\approx 20Mpc/h$ and with the size of $187Mpc/h$ centered in the AMR region. The renderings are done with Visivo (Comparato et al.2007, <http://visivo.cineca.it>).*Right*: 3-D distribution of Dark Matter density inside the AMR region (the side of the image is $\approx 8Mpc/h$) at $z = 0$.

volume is $\sim 480^3(Mpc/h)^3$ for the whole cluster sample. This initial set of simulations was used to find the most massive clusters in the volume, targets of the re-simulations at higher spatial and mass resolution.

The most massive objects of all boxes were identified with an halo finder algorithm working on gas/DM spherical over-density (e.g. Gheller, Pantano & Moscardini 1998). Nested initial conditions were then applied to the volumes comprising the formation regions of all clusters, to achieve a higher DM mass resolution for the cosmic volume involving the formation of the clusters. In details, two levels of nested initial conditions were placed in cubic regions centered on the cluster centers. After a few tests, we adopted the combination of grid sizes which resulted to be the best compromise between the computational cost and the need for the best possible resolution in the cluster volumes.

The first level box had the size of $\approx 95Mpc/h$ (with $m_{dm} \approx 5.4 \cdot 10^9 M_\odot/h$ and constant spatial resolution of $\Delta_1 \approx 425kpc/h$). The second had a size of $\approx 47.5Mpc/h$ (with $m_{dm} \approx 6.7 \cdot 10^8 M_\odot/h$ and constant spatial resolution of $\Delta_1 \approx 212kpc/h$). For every cluster run, we identified cubic regions with the size of $\sim 6R_v$ (where R_v is the virial radius of clusters at $z = 0$, calculated on lower resolution fast runs), and allowed the code to apply 3 additional levels of mesh refinement, achieving a peak spatial resolution of $\Delta \approx 25kpc/h$; in the following, we will refer to

this sub-volume as to the “AMR region”.

From $z = 30$ (initial redshift of the simulation) to $z = 2$, mesh refinement is triggered by gas or DM over-density criteria. From $z = 2$ an additional refinement criterion based on 1-D velocity jumps (Va09) is switched on. This second AMR criterion is designed to capture shocks and intense turbulent motions in the ICM out to the clusters outskirts. The reader can refer to Va09 and VGB10, where we presented a detailed comparison of the differences in the properties of thermal gas, shocks and turbulence distributions found when comparing the standard and the our extended mesh refinement method.

Compared to the standard mesh refinement strategy, we showed that the use of the additional refinement on velocity jumps leads to:

- a sharper reconstruction of accretion and merger shocks in the clusters volume;
- a ~ 10 percent lower gas density and a ~ 10 per cent larger gas entropy profile inside the clusters core;
- a substantially enhanced presence of turbulent motions at all radii (up to a factor ~ 2 in energy);
- a more efficient mixing of gas matter during the whole cluster evolution.

All these results are well converged for re-simulations adopting a threshold value of $\delta v/v \leq 3$ to trigger the mesh

refinement locally, where δv is the 1-D velocity difference and v is the minimum velocity for the cell in the patch of cells to be refined (converge tests can be found in Va09).

We also note that recent works (e.g. Agertz et al.2007; Wadsley et al.2008; Springel 2010; Robertson et al.2010) suggested that Eulerian codes can be subject to considerable un-physical numerical diffusion, that may lead to a suppression of fluid instabilities, in the regions where the mesh resolution is too low and large bulk motions are present. However, the opportune triggering of mesh resolution in these regions, such that implemented in our cluster runs, can overcome this problem (Robertson et al.2010).

In the cluster runs presented here, the number of cells refined up to the peak resolution ($25kpc/h$) at $z = 0$ varies from ~ 20 to ~ 40 per cent of the total volume within the AMR region ($N \sim 10^7 - 10^8$ cells). In Fig.1 we show the map of the spatial distribution for the refinement levels, with overlaid contours of gas temperature, for two representative clusters of the sample.

Approximately, the number of high resolution DM particles contained within the AMR region at $z = 0$ is of the order of $N_{dm} \sim 2 - 3 \cdot 10^7$, and only a few (< 100) DM particles coming from the lower resolution regions are found (but never within the virial volume of clusters). However, the gravitational potential in the PM approach is computed after interpolating the DM mass distribution onto a grid, and no problems of contamination (leading, for instance, to a spurious transfer of kinetic energy) are present.

Figure 2 shows a rendering of the 3-D distribution of gas matter within the whole computational region of side $187Mpc/h$, and a zoom into the sub-volume of $\approx 13.6Mpc/h$ of the AMR region for one of the cluster run.

Our runs neglect radiative cooling, star formation processes and AGN-feedback. Re-heating due to stars and AGN activity is treated at run-time with a simplified approach reproducing an Haardt & Madau (1996) re-ionization model. A detailed description is reported in the Appendix A.

Figure 3 shows a slice in gas temperature for the biggest cluster in our sample (E18A), giving the visual impression of the extraordinary amount of details characterizing each simulated cluster at $z = 0$: gas substructures, sharp

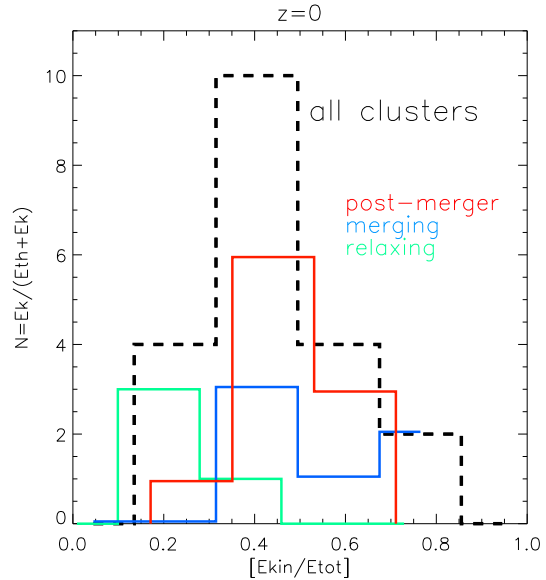


Figure 5: Distribution for the ratio between the total kinetic energy, E_{kin} and the total energy (thermal+kinetic), E_{tot} , within the virial volume each cluster in the sample (dashed line). In colors, we additionally show the distribution of the energy ratio for the three classes of clusters discussed in the paper.

shock discontinuities and various kinds of fluid instabilities (e.g. Kelvin-Helmoltz and Rayleigh-Taylor) can be easily found at all distances from the cluster core to the most peripheral regions, with similar resolution.

Approximately, every cluster run took ~ 30000 cpu hours on a linux SP6 cluster at CINECA (Casalecchio di Reno, Bologna), for a total amount of $\sim 8 \cdot 10^5$ hours of CPU time. One of the future goal of this project is to apply tracer particles in the study in the ICM. To make this possible in a post-processing phase (as in VGB10), for every cluster we saved a large number of time outputs (between 60 and 90), with an approximate time sampling of $0.1Gyr$ for $z < 1.0$. This huge amount of data will allow the users for a number of iterative studies (e.g. focusing on Cosmic Rays injection and advection in the ICM), without having to run the simulations again.

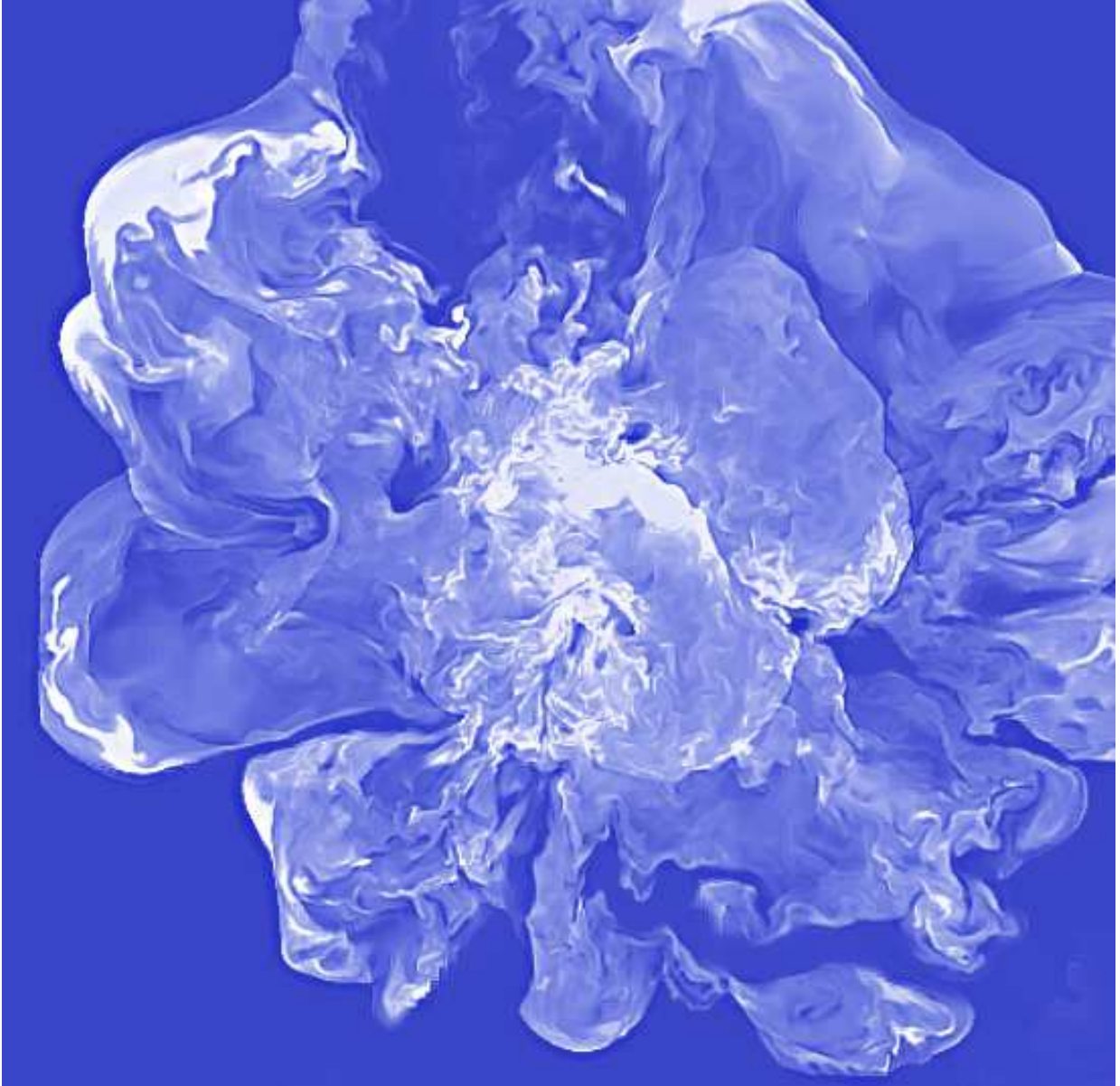


Figure 3: A slice in gas temperature for the most massive cluster in our sample, E18A, at $z = 0$. The resolution of the image is $25kpc/h$ per pixel, the size of the image is $13.6Mpc/h$. The underlying structure of mesh refinements levels is sketched in the right panel of Fig.1.

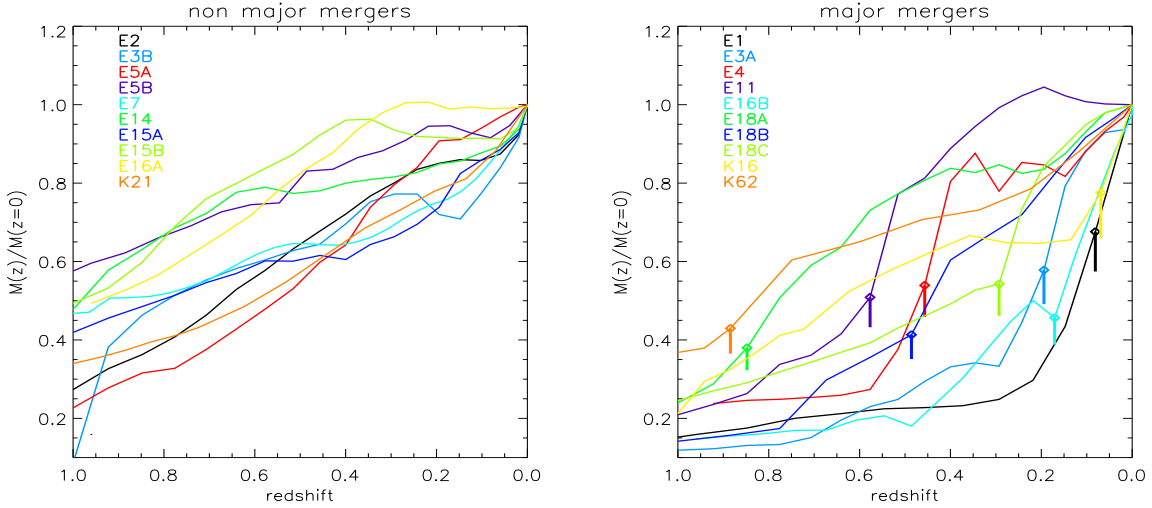


Figure 4: Evolution of the total virial mass for all clusters in the sample, normalized for the total mass at $z = 0$. The *left* panel shows the evolution for *non-major merger* clusters, while the *right* panel shows the evolution for *major merger* clusters; additional arrows show the approximate epoch of the last major merger event for every object.

2.3. The clusters sample

Table 1 lists all the simulated clusters, along with their main parameters described here below. All the objects have a total mass $M > 6 \cdot 10^{14} M_{\odot}$, 12 of them having a total mass $M > 10^{15} M_{\odot}$.

This makes our simulated sample a unique tool to study the evolution of the richest cluster of galaxies in the Universe, in an evolving cosmological framework.

In order to classify the clusters according to their dynamical state, we adopted two independent proxies computed for each cluster, in order to account for their main dynamical differences at $z = 0$.

First, we followed in detail the matter accretion history of all clusters, in the range $0 \leq z \leq 1$. In Fig.4 we show the total (DM+gas) mass evolution for every object, as reconstructed using the lower mesh refinement level in the AMR region ($\Delta \approx 200 kpc/h$). The clusters can be broadly grouped into two categories depending on the presence of a major merger event for $z < 1$ epochs (in the following we will conventionally use the terms of “major merger” or “relaxing” cluster for the two categories).

A major merger is defined as a total matter accretion episode where $M(t_2)/M(t_1) - 1 > 1/3$ (e.g. Fakhouri,

Ma & Boylan-Kolchin 2010); in our case, we fixed $t_2 = t_1 + 1Gyr$. The time resolution of $1Gyr$ is of the order of the crossing time within the virial volume of clusters, and our tests showed that it is small enough to capture the sharp increase of cluster mass during strong mergers.

In the last column of Tab.1 we report the approximate epoch of the last major merger event for major merger objects of the sample; this procedure divides our total sample in two equal classes of 10 objects each.

We noted, however, that the analysis of the matter accretion history for the virial volume is not sensitive enough to account for the possible variety of cluster morphologies. This is the case of clusters experiencing the early stage of a strong merger event (i.e. “merging” systems), that can make their overall morphology significantly asymmetric and perturbed even if the total mass has not yet increased in a significant way.

For this reason, we computed a second, independent proxy of the dynamical state of each cluster, measuring the ratio between the total kinetic energy of gas motions inside the virial region, E_{kin} , and the thermal (thermal plus kinetic energy), inside the virial volume at $z = 0$. The results are reported in the 4th column of Tab.1. The kinetic

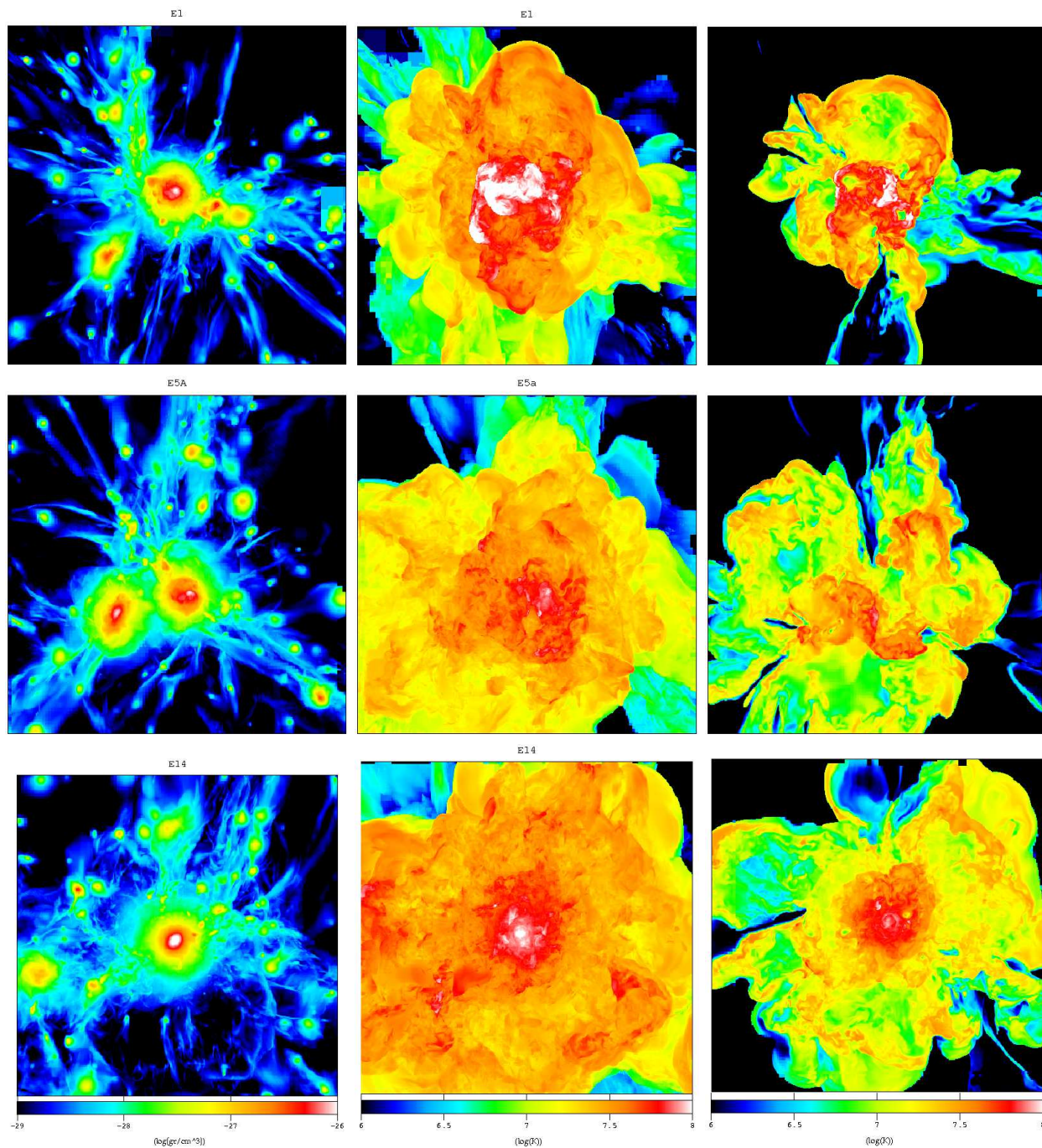


Figure 6: The visual appearance of the three categories of clusters considered in the paper. *Top* panels: the major merger cluster E1; *center* panels: the merging cluster E5A; *bottom* panels: the relaxing cluster E14. From right to left, shown are: maximum gas density along the line of sight (*left column*); maximum gas temperature along the line of sight (*center column*) and gas temperature in a slice of depth 25kpc/h (*right column*). The side of each image is $\approx 13.6\text{Mpc}/h$.

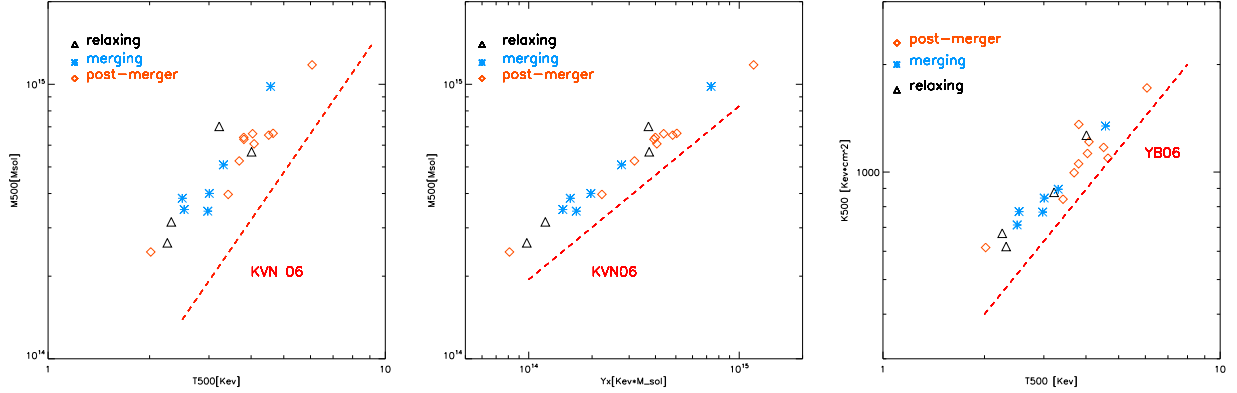


Figure 7: Scaling relations for all clusters in the sample at $z = 0$. *Left panel*: M_{500} versus T_{500} relation, the additional dashed line is for the fit relation reported in Kravtsov, Vikhlinin & Nagai (2006). *Central panel*: M_{500} versus Y_{500} (gas pseudo-pressure) relation, the additional red line shows the “perfect-slope” scaling (Kravtsov, Vikhlinin & Nagai 2006). *Right panel*: S_{500} (gas entropy) versus T_{500} relation, the additional red line shows the scaling obtained by Younger & Bryan (2006).

energy of each cluster has been computed after subtracting the velocity of the center of (total) mass from the 3-D velocity field. This parameter provides an indication of the dynamical activity of a cluster associated to the overall amount of mergers (e.g. Tormen, Bouchet & White 1997; Vazza et al. 2006). However, this procedure may be affected by the presence of massive companions in major merger systems, since this would bias somewhat the estimate of the center of mass of the main cluster. Nevertheless, $X = E_{kin}/E_{tot}$ provides a meaningful estimate of *perturbed* system in a statistical sense, while in some particular cases the value may be underestimated by the error involved in the center of mass estimate. Indeed, Fig. 5 shows that major merger systems statistically present a large value of this ratio, with $X \geq 0.4$ in most of objects (with a maximum of $X \sim 0.8$ in 2 cases). In what follows, we will define as “merging systems” those objects that present a $X > 0.4$ value, but did not experienced a major merger in their past, according to the previous definition.

According to the above classification scheme, our sample presents 4 “relaxing” objects (clusters with no strong merger for $z < 1$), 6 “merging” objects (clusters at the early stage of a merger with a massive companion inside the AMR region) and 10 “major merger” objects (clusters with a $M(t_2)/M(t_1) - 1 > 1/3$ for $z < 1$).

In Fig. 6 we give a visual representation of 3 clusters

representative of the above dynamical classes, mapping in the plane of the image the the maximum of gas density along the line of sight, the maximum temperature along the line of sight and the gas temperature for a slice crossing the center of each cluster.

The major merger cluster E1 (first row) presents a richness of gas substructures and the imprints of strong shock heating as a result of the major merger event that the cluster experienced at $z \sim 0.1$. Also, the slice in gas temperature clearly unveils the presence of a cold front in the cluster center, likely located in the core of the accreted satellite.

The merging cluster E5A is characterized by a quite smooth distribution of gas temperature, but with the asymmetric imprint of a large scale accretion due to the in-falling companion, whose center is located at the distance of $\sim 3 Mpc$ from the center of E5A.

The relaxing cluster E14 presents a quite regular distribution of gas temperature and gas density, which approaches spherical symmetry in the innermost region, and it is characterized only by minor accretion episodes.

The complete visual survey of all the clusters in the sample is reported in the Appendix (B).

2.4. The IRA-CINECA Archive

The results of our simulation, in terms both of raw outputs and of post-processed data, have features that make them interesting to a broad “audience”. The high spatial resolution and numerical accuracy, the large number of available redshift outputs (time resolution), and the large number of clusters (statistics) can be exploited for different purposes, similar or even different from the original objectives.

Consequently, most of the produced data have been openly published and are available through the web portal <http://data.cineca.it>, in the *IRA-CINECA Simulated Cluster Archive* section. The direct outputs of the simulations are available, in a reconstructed (i.e. monolithic 3–D boxes of the various gas/DM fields) or in the native ENZO domain-decomposed formats. In both cases, the files adopt the HDF5 standard. For most of the clusters in the sample, the whole evolution of ENZO outputs (one every two time-steps) is available from $z = 1$ to $z = 0$, making possible a highly resolved ($\Delta t \sim 0.1\text{Gyr}$) time study of the clusters evolution in all gas/DM fields. In addition, the set of nested initial conditions for all clusters in the sample is provided in the same repository, along with preliminary reduction of data and processing pipelines.

Due to the complexity and the size of our data products, they have been organized and managed by means of a specialized software: iRODS (integrated Rule Oriented Data System - <http://www.irods.org>) a data grid software system developed by the Data Intensive Cyber Environments (DICE) research group at the University of North Carolina at Chapel Hill and the Institute for Neural Computation (INC) at the University of California, San Diego.

We have exploited a few of the most interesting features of iRODS. The data have been organized according to a specialized directory hierarchy and they have been described by a precise data model in terms of associated meta-data. The details can be found in a dedicated paper (Gheller et al. in preparation). Part of the meta-data is managed directly by the iRODS integrated iCAT database (PostgreSQL based), while part of it requires the adoption of a simple complementary relational database. This is due to the current limitations of iCAT, which, however are expected to be overcome in the next iRODS release, leading to a more homogeneous treatment of metadata. The metadata can be used both to retrieve information

about the corresponding data objects and to perform SQL based search, which allows the users to explore efficiently and effectively the data archive, rapidly discovering the data sets of interest.

The iRODS server runs on the CINECA’s SP6 HPC system, where the data was produced and is currently stored. This, in order to avoid expensive and potentially unsafe (for data integrity) data transfers across different storage devices. The native support of iRODS for multi-streaming data transfer protocols (e.g. GridFTP) will be exploited to deploy high performance download services, necessary to move huge data objects. Finally, the possibility of federating geographically distributed data servers, may, in the future, be exploited to mirror the data and make its access even more effective.

At the time of the submission of the present paper, only a few of such services are available, being still in a development or consolidation phase. However, data are available and can be obtained on request, following the instructions posted on the web portal.

The authors encourage the public access of data and the use of them for original scientific research and mutual collaboration. *If a paper is published with simulations produced in this project, the authors should cite the present paper, and acknowledge the support of the public archive at CINECA.*

3. Results

3.1. Thermal properties: scaling laws

It is well known that non-radiative simulations like those we report here, present important differences compared to real clusters, and compared to cluster simulations with radiative cooling (e.g. Borgani et al.2008 for a review). However, the most significant differences are found for halos with masses and temperature lower than those considered in this work (e.g. for clusters with $T_{500} < 1\text{keV}$), and therefore our clusters are expected to provide a viable representation of non cool-core systems.

As a first consistency check of the results produced by our cluster runs, we computed the integrated values of M_{500} , T_{500} , S_{500} and Y_X for all clusters, where M_{500} is

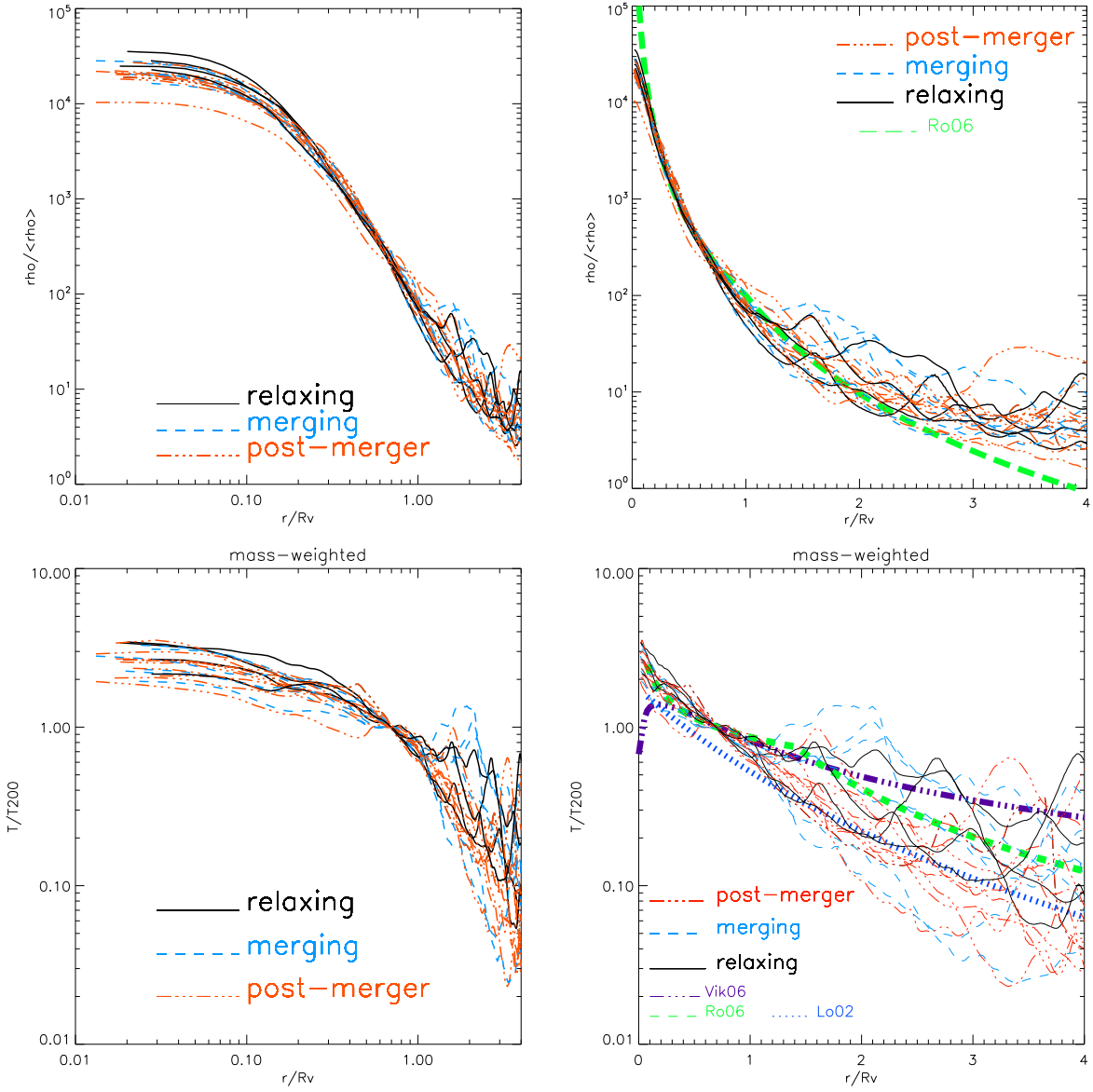


Figure 8: Radial profiles of gas density (top panels) and gas temperature (bottom panels) for the clusters in the sample at $z = 0$, with two different spacings for the X-variable. The different type of lines refer to clusters in a different dynamical state, according to Sec.2.3. The additional lines are for the fit relations presented by: Roncarelli et al.(2006) as *green lines*, Vikhlinin et al.(2006), as *purple line* and Loken et al.(2002), *blue line*.

the total (gas+DM) mass inside r_{500} ¹, T_{500} and S_{500} are the the mass weighted temperature and mass weighted entropy (where the entropy is customary defined as $S = T/\rho^{2/3}$) at the same radius, and Y_X is the cluster total projected-pressure (Kravtsov, Vikhlinin & Nagai 2006), measured as $M_{gas,500} \cdot T_{500}$, where $M_{gas,500}$ is the gas mass inside r_{500} .

The panels in Fig.7 show three meaningful scaling laws for galaxy clusters studies: the T_{500} versus M_{500} , the Y_X versus M_{500} and the T_{500} versus S_{500} scaling laws.

The (T_{500}, M_{500}) relation presented in the first panel in Fig.7 shows that our clusters follow the same scaling as in the self-similar model, $M_{500} \propto T_{500}^{3/2}$ (e.g. Kravtsov, Vikhlinin & Nagai 2006), which is also consistent with Chandra or XMM-Newton observations of massive galaxy clusters (e.g. Vikhlinin et al.2005). The systematic bias of ~ 30 per cent in the vertical direction is mainly due to the discrepancy between the real cluster mass measured in 3-D simulations and the derivation of mass from real clusters, under the hypothesis of hydrostatic equilibrium (e.g. Rasia et al.2006; Piffaretti & Valdarnini 2008).

The (Y_X, M_{500}) relation reported in the second panel in Fig.7 is expected to be the clusters scaling relation subject to the smallest intrinsic scatter (e.g. “the perfect slope”, Kravtsov, Vikhlinin & Nagai 2006). Indeed, our clusters follows the $M_{500} \propto Y_X^{3/5}$ scaling with an extremely small scatter across one order of magnitude in Y_X . The vertical systematics can be explained as in the previous case.

The (T_{500}, S_{500}) relation (third panel in Fig.7) for our clusters closely follows the self-similar prediction $S_{500} \propto T_{500}$ (e.g. Voit et al.2005). In the figure we show as a comparison the results obtained by Younger & Bryan (2006) with an earlier version of the ENZO code (and in the case of no pre-heating of the ICM). The origin for the ~ 10 per cent bias in the entropy at r_{500} is likely to be due to the slightly larger amount of entropy production (or entropy mixing) observed when standard mesh refinement is supplemented with the extra refinement triggered by using also velocity jumps, as shown in VGB10.

Our data proved to be compatible with the expected

¹ r_{500} is defined as the radius enclosing a mean cluster density of 500 times the critical density of the Universe; for the assumed cosmological model this radius correspond to $\approx 0.5R_v$.

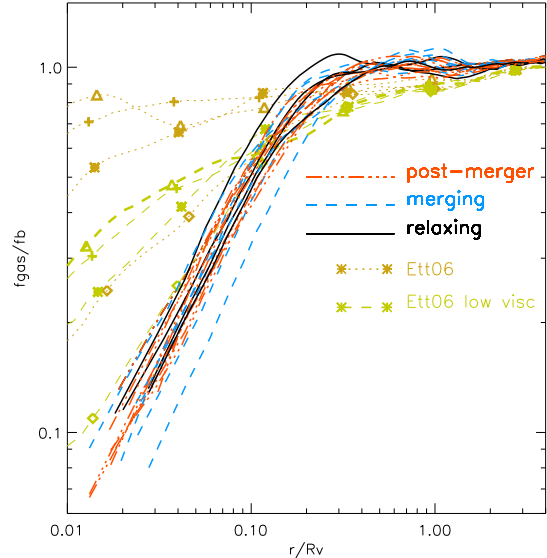


Figure 9: Radial profiles of gas baryon fraction for the clusters in the sample at $z = 0$. The additional lines are for 4 galaxy clusters produced with GADGET2, with standard viscosity (dotted lines) or a reduced viscosity scheme (dashed lines), as reported in Ettori et al.(2006).

scaling relations, and this suggests that the global properties of our sample of clusters provide a meaningful statistical representation of the most massive galaxy clusters in the Universe at $z = 0$.

3.2. Thermal properties: radial profiles

The high spatial resolution available in the peripheral regions of our massive galaxy clusters ($\approx 25kpc/h$ up to a distance of $8 - 10Mpc$ from the centers of clusters) provides a unique possibility of characterizing the thermal properties of the clusters accretion regions using cosmological numerical simulations with respect to what previously done in the literature.

In the case of Smoothed Particles Hydrodynamics simulations of galaxy clusters, the extremely high spatial resolution achieved in cluster cores (e.g. $\Delta \sim 5 - 10kpc$) is quickly lost approaching the virial radius, due to the variable smoothing length (e.g. $\Delta > 200kpc$), and makes it difficult to obtain highly accurate spatial information for the cluster peripheral regions (e.g. Frenk et al.1999;

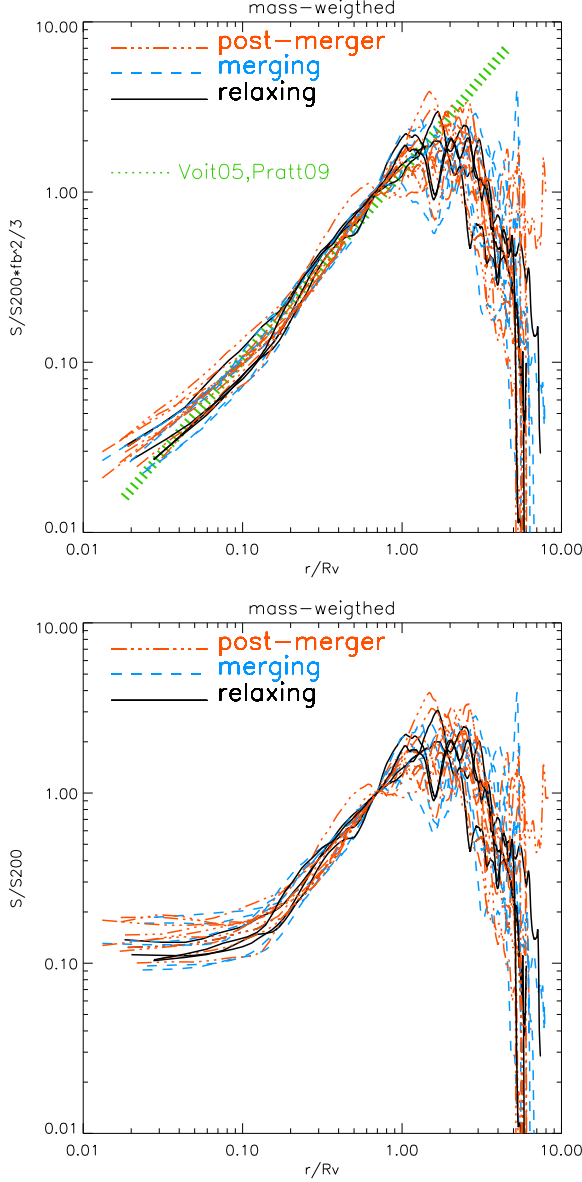


Figure 10: *Top panel*: gas entropy radial profiles normalized by the baryon fraction within the same radius, as suggested by Pratt et al.(2009). The additional line is the best fit from Voit et al.(2005).*Bottom panel*: gas entropy profiles normalized by their value at r_{500} .

O’Shea et al.2005); a similar effect is also present in Eulerian simulations employing standard AMR techniques (e.g. Va09).

Also the information from present X-ray observations of clusters is typically limited to the innermost cluster regions (e.g. $r < 0.5R_v$) and only very recently the SUZAKU satellite made possible to obtain radial information out to larger radii for a few clusters (e.g. George et al.2009; Reiprich et al.2009; Bautz et al.2009; Hoshino et al.2010; Kawaharada et a.2010).

In Fig.8 we show the gas density and temperature profiles, centered on the center of total mass (gas+DM) of each object. All radii were normalized to the virial radius of each cluster, while values of density and temperature were normalized to their values at R_{200} , R_{200} being the radius inside which the mean density of the cluster is 200 times the critical density of the Universe ($R_{200} \approx 0.7R_v$).

The results are shown using both a logarithmic scale (*left panels*) to highlight the behavior in the innermost cluster region, and linear scale (*right panels*), in order to emphasize the large scale trends. In most of cases, the profiles present the evident imprints of massive and hot structures in the outer ($> 2R_v$) regions, and in this respect the classes of objects are characterized by a similar degree of fluctuations. In the right panels of Fig.8, we additionally over-plot as a comparison the average behavior reported in Roncarelli et al.(2006)² for a sample of 7 galaxy clusters (4 with total masses larger than $10^{15}M_\odot$) simulated with GADGET2 (Springel 2005). The profiles from Roncarelli et al.(2006) fall within our cluster statistics for $r < 2R_v$. However, since they focused on the *smooth* gas component of the cluster matter (which implied a filtering out of gas substructures at all radii), the larger mean density of our profiles at outer radii is easy explained by the contribution of gas cumps/filaments in our procedure.

We conclude that the average radial behavior of gas density and gas temperature for our clusters is consistent with the other works in the literature which used complementary numerical approaches to produce cosmological simulations of galaxy clusters. On the other hand, our simulations provide an unprecedented look at those external cluster regions. Large fluctuations in gas temperature

²In Roncarelli et al.(2006) the best fit of gas density and gas temperature profile is performed within the range of $0.3 \leq r/R_{200} \leq 2.7$.

can be observed, and these features can be explained as the combined effect of having more resolved shock waves, and more resolved accretion patterns around in-falling satellites. For instance, strong non-radiative shocks produce a post-shock density enhancement of a factor 4, and an enhancement in temperature which scales with M^2 (M is the shock Mach number), and therefore resolved shock structures in our simulations produce sharp positive contribution to the mean radial density or temperature profiles.

Indeed, if we compare with previous results obtained by Loken et al.(2002) using a early version of the ENZO code with standard mesh refinement (dotted blue line in the bottom right panel of Fig.8), we note that all radii our profiles show a slightly larger normalization and a larger amount of structures in temperature. This is consistent with the presence of high-temperature regions associated with strong and well-resolved pattern of accretion shocks in the outer atmosphere of our clusters, which are otherwise spread over larger distances if an overdensity-based refinement alone is applied (e.g. Skillman et al.2008).

In Fig.8 we also over-plot the mean temperature profile reported by Vikhlinin et al.(2006) from CHANDRA observations, and its extrapolation at large scale. At large radii ($r > R_v$) the simulated clusters show a steeper temperature profile compared to the extrapolated values from the fitting formula of Vikhlinin et al.(2006):

$$T(r) \propto \frac{[(x/0.045)^{1.9} + 0.45]}{[(x/0.045)^{1.9} + 1] \cdot [1 + (x/0.6)^2]^{-0.45}}, \quad (1)$$

where $x = r/r_{500}$. Differently from the case of central cluster regions, the behavior of temperature at these density regimes is expected to be mostly unaffected by any additional implementation of physical processes (radiative cooling, star formation etc.), and therefore this should be a general trend of Eulerian simulations. However, the contamination of in-falling substructures at all radii leads to a large degree of scatter in our data. The presence of particular direction of matter accretion (such as cosmic filaments) may also make the large scale distribution of temperature highly asymmetric, explaining why the differences in the profiles of clusters with similar masses. Interestingly enough, the presence of a filamentary structure of galaxies was recently suggested by Kawaharada

et al.(2010) to explain the observed large scale temperature anisotropy in a cluster Abell 1689, observed with SUZAKU.

In Fig.9 we show the radial profiles of the enclosed baryon fraction, f_{gas} , for every cluster in the sample. The baryon fraction is normalized to the cosmic baryon fraction, f_b . As expected, f_{gas}/f_b reaches the value of ≈ 1 at the virial radius of the clusters, with a scatter < 10 percent when *relaxing* and *merger* (or *merging*) clusters are compared.

The issue of the gas fraction distribution in galaxy clusters has been extensively studied with numerical simulations in the last few years, reporting small but systematic differences between Eulerian and Lagrangian approaches (e.g. Borgani et al.2008 and references therein). In particular, the gas fraction inside the virial radius of clusters was found to be systematically higher (~ 10 percent level) in Eulerian AMR runs, compared to SPH runs (e.g. Ettori et al.2005; Kravtsov et al.2006).

We compare our profiles with the profiles of 4 galaxy clusters within a similar mass range, taken from Ettori et al.(2006). The dotted lines are for GADGET2 simulations using the standard formulation for the artificial viscosity (e.g. Springel 2005), while the dashed lines are for the simulations of the same clusters adopting a reduced viscosity formulation (Dolag et al.2005). In all cases GADGET runs show larger baryon fraction within the core region of clusters, although in the case of low-viscosity results the profiles approach the ENZO-AMR runs. In ENZO PPM no artificial viscosity (beside the *numerical one*) is present and due to our mesh refining procedure the effect of shock waves and turbulent motions is maximized. We can thus speculate that the basic difference in the inner profile of baryon fraction between SPH and grid simulations is mainly due to the differences in mixing and stripping of accreted satellites in the two schemes (as early pointed out in Frenk et al.1999), which are both affected by the presence of viscous forces in the simulations. In runs without viscosity (PPM scheme or SPH with reduced artificial viscosity) the stripping of in-falling sub clumps is more efficient (e.g. ZuHone, Markevitch & Johnson 2009) and the stripped gas is distributed to larger radii compared to runs with physical viscosity.

In the top panel of Fig.10 we show the entropy pro-

files, $S \equiv T/\rho^{2/3}$ (normalized by the value at r_{200}) for our clusters, multiplied by the baryon fraction inside the same radius. As recently suggested by Pratt et al.(2009), an universal profile may exist for $S \cdot f_{gas}^{2/3}$, both in the case of cool-core and non cool-core clusters. This may be explained by a scenario in which the feedback mechanism responsible for the increase of entropy in the innermost region of some galaxy cluster (e.g. AGN activity), also affects the radial distribution of baryon gas at the same level. Therefore the product of the two quantity levels out the two effects and the resulting profile is similar, regardless of the activity of a feedback mechanism. Our data present a very good agreement with the reported correlation. This is also consistent with the (T_{500}, S_{500}) scaling relation already discussed in Sec.3.1.

In the bottom panel of Fig.10 we show the entropy profile for each cluster (normalized to their value at r_{200}). All our clusters, almost independently with their dynamical state, show a well-defined flattening of the entropy distribution inside $< 0.1R_v$.

Eulerian simulations of galaxy clusters are generally known to convey higher amount of entropy in the center of non-radiative galaxy clusters, by the combined effect of more efficient shock heating and mixing motions, compared to SPH (Wadsley et al.2008; Mitchell et al.2009). Similar results for re-simulations of galaxy clusters of intermediate masses ($M \leq 3 \cdot 10^{14} M_{\odot}$) were reported in VGB10 using the same methods as in the present work.

Given the large resolution and the high number of clusters available in this sample, we confirm this trend also in a statistical sense, reporting that *all* simulated galaxy clusters present a well developed entropy core, with the size of $\sim 0.1R_v$, with no evident relation with their dynamical state. This is of the order of $200 - 300kpc$, which is much larger than the softening length for the calculation of the gravitational force in the PM scheme adopted by ENZO; therefore the entropy core found in our simulations is not a numerical artifact. Therefore, it would be interesting to apply more complex models of the innermost cluster regions (e.g. by adopting cooling, AGN feedback, etc) in order to measure the requested amount of extra-heating budget to quench catastrophic cooling, for the level of entropy mixing modeled by these cluster simulations.

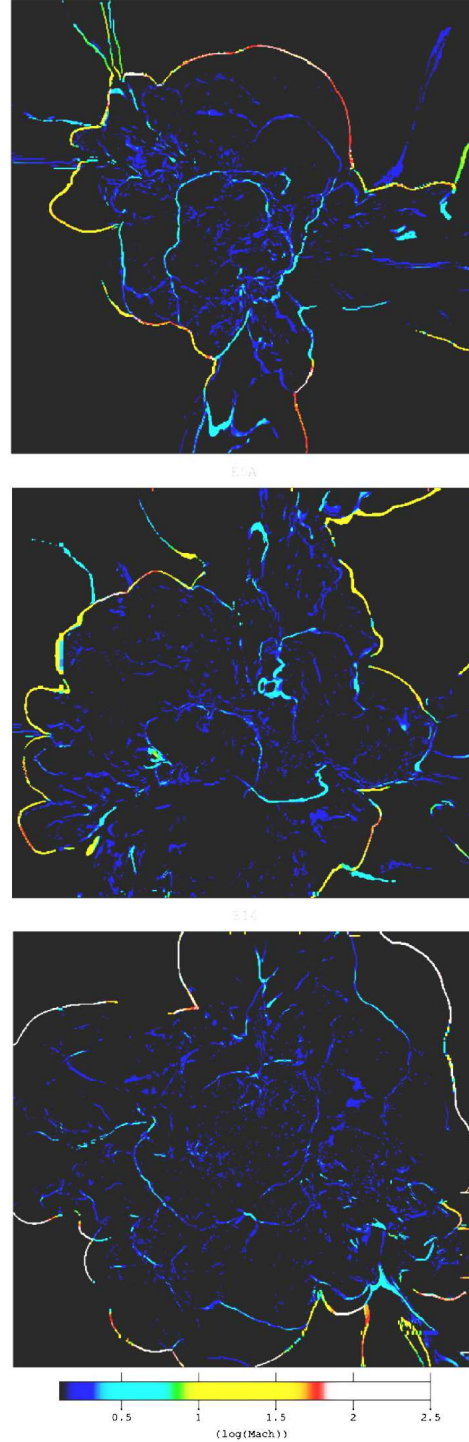


Figure 11: Slices showing the Mach number of shocked cells for the same clusters and regions as in Fig.6: E1 (Top), E5A (center) and E14 (Bottom).

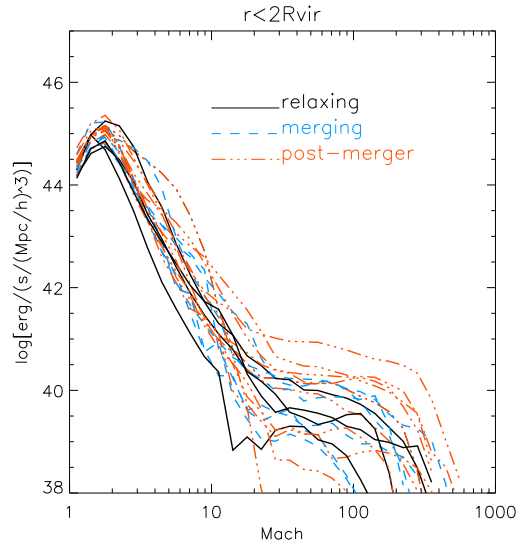
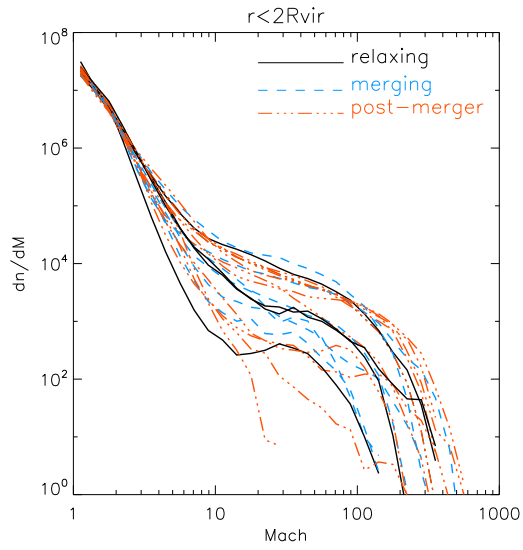
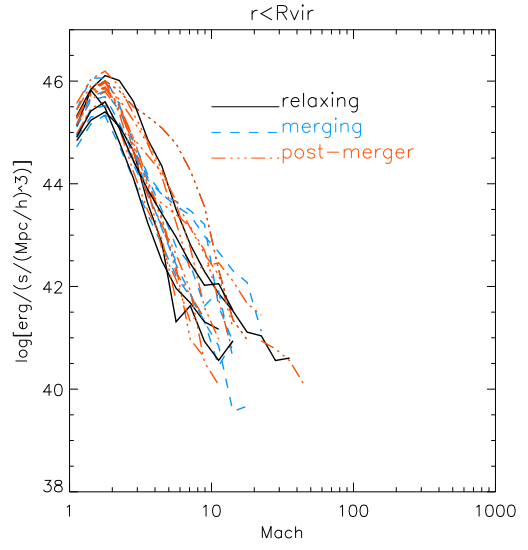
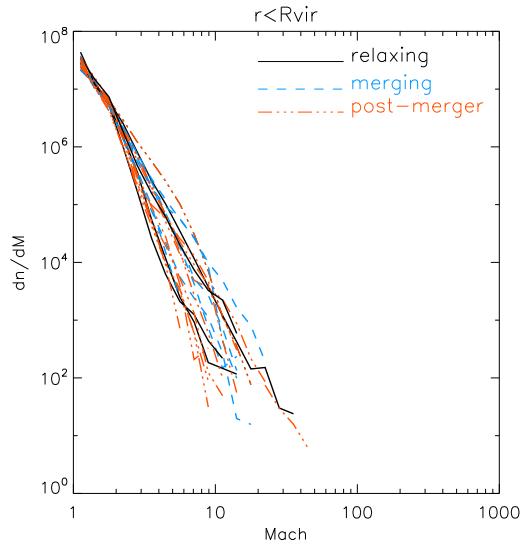


Figure 12: Number distributions of shocked cells for $r < R_v$ and $r < 2R_v$ volumes.

Figure 13: Thermal energy flux distributions of shocked cells for $r < R_v$ and $r < 2R_v$ volumes.

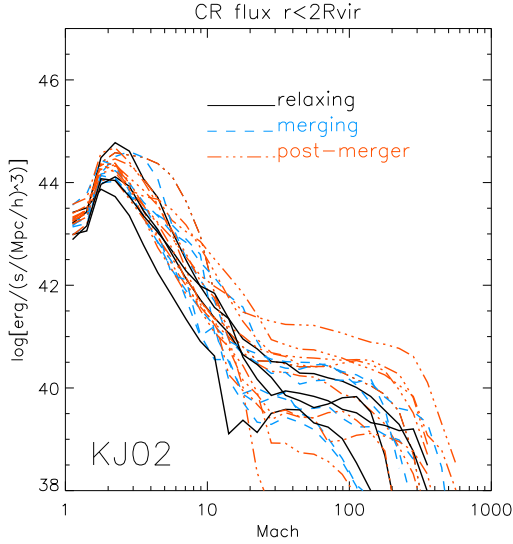


Figure 14: Cosmic Rays energy flux distributions for $r < 2R_v$, obtained with the injection model of Kang & Jones (2002).

3.3. Shock Waves.

Our clusters sample is well suitable to study shocks statistics in the cluster formation region even at large radii from the clusters center, since the refinement scheme presented in Va09 preserves the peak resolution of $25kpc/h$ on all shock features within the AMR region.

Observationally, merger shocks have been detected only in a few nearby X-ray bright galaxy clusters (Markevitch et al.2005; Markevitch 2006; Solovyeva et al.2008). They may be associated with single or double radio relics discovered in a number of galaxy clusters (e.g. Roettgering et al.1997; Markevitch et al.2005; Bagchi et al.2006; Giacintucci et al.2008; Bonafede et al.2009). Shocks in large scale structures have been investigated in a number of semi-analytical (Gabici & Blasi 2003; Berrington & Dermer 2003) and numerical works (Miniati et al.2001; Ryu et al 2003; Pfrommer et al.2007; Hoeft et al.2008; Skillman et al.2008, Vazza et al.2009; Molnar et al.2009).

We identified shocks with the same procedure presented in Vazza, Brunetti & Gheller (2009), based on the analysis of velocity jumps across close cells. The preliminary selection of candidate shocked cells is made from the requirement that $\nabla \cdot \mathbf{v} < 0$; the Mach number is finally

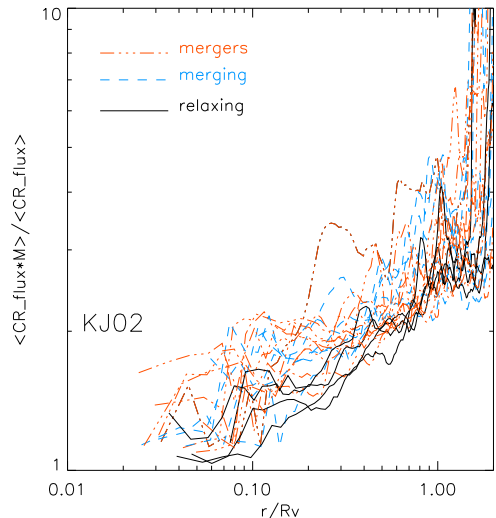
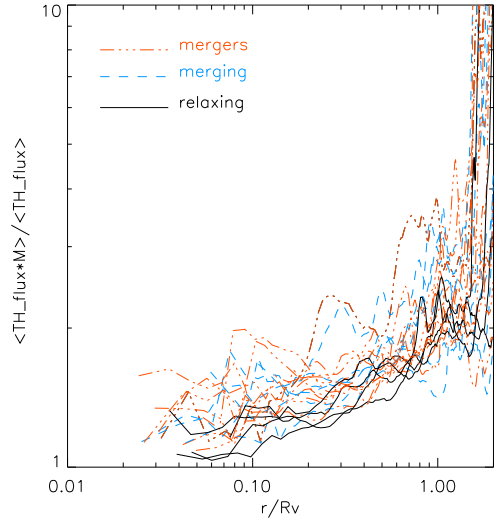
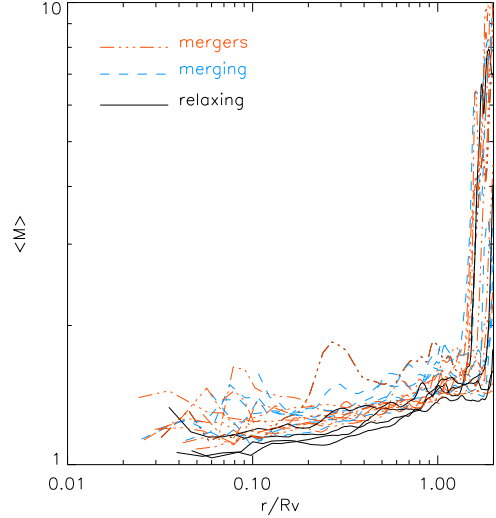


Figure 15: Profiles of volume-weighted mean Mach number (top panel), thermal flux weighted mean Mach number (middle panel), CR-flux weighted mean Mach number (bottom panel) for the injection model of Kang & Jones (2002).

evaluated from the inversion of:

$$\Delta v = \frac{3}{4} c_s \frac{1 - M^2}{M^2}, \quad (2)$$

where Δv is the 1-D velocity jump between 3 cells across the candidate shock, and c_s is the sound speed of the cell with the minimum temperature. The full 3-D Mach number is then recovered as $M = (M_x^2 + M_y^2 + M_z^2)^{1/2}$.

The panels in Fig.11 show the map of shock Mach numbers for the clusters E1, E5A and E14, taking the same slices as in the Right column of Fig.6. The differences in cluster dynamics translate also in significantly different large scale patterns of shock waves: a quite irregular and asymmetric pattern of external shocks is observed in the case of the merging cluster E5A. Also a few merger shocks can be found in the virial region region of clusters E1 and of E5A, while in the case of E14 only weak shocks can be found inside the cluster core.

Following Vazza, Brunetti & Gheller (2009) we calculated the volume distribution of shocks as a function of M . This is shown in Fig.12, for $r < R_v$ and $r < 2R_v$. Both distributions are steep, with an average slope of $\alpha \sim -4 \div -5$ (with $\alpha = d \log N(M) / d \log M$) for $M < 10$, consistently with results obtained with earlier results obtained with ENZO at fixed grid resolution (Vazza, Brunetti & Gheller 2009). When the shocks distribution is computed for $r < 2R_v$, the differences among clusters is found to be larger, especially for strong shocks with $M > 10$.

This simply mirrors the scatter in the temperature distributions reported in Sec.3.2.

The thermal energy flux across shocked cells is evaluated with

$$f_{th} = \delta(M) \cdot \rho M^3 v_s^3 / 2, \quad (3)$$

where ρ is the pre-shock density and $\delta(M)$ is a monotonically increasing function of M (e.g. Ryu et al.2003).

Figure 13 shows the thermal energy flux distributions as a function of the Mach number, for $r < R_v$ and $r < 2R_v$. The thermal energy flux for each cluster has been rescaled assuming the volume of a sphere of radius $\sim R_v = 3Mpc$ in order to highlight the trend only due to cluster dynamics. Both distributions present a well defined peak of maximum thermalisation at $M \approx 2$, and are very steep for all clusters: $\alpha_{th} \approx -5$ (with α_{th} taken as $f_{th}(M)M \propto M^{\alpha_{th}}$),

in agreement with results based on fixed grid resolution runs, reported in Vazza, Brunetti & Gheller (2009).

Results based on SPH (Pfrommer et al.2007) show significantly flatter distributions ($\alpha_{th} \approx -3$ to -4), while in our sample this can be found only for a few clusters subject to violent merger events. Also in this case, the larger differences among our sample are found for $M > 10$ shocks external to R_v , and usually ~ 10 times more energy is processed by these shocks in the case of post-merger systems, compared to the relaxing ones.

We apply also a simple recipe to estimate the efficiency of injection of Cosmic Rays protons at shocks, with a standard application of the Diffusive Shock Acceleration theory (e.g. Kang & Jones 2002, hereafter KJ02). The adopted injection efficiency is a function of the Mach number only:

$$f_{CR} = \eta(M) \cdot \rho M^3 v_s^3 / 2; \quad (4)$$

where $\eta(M)$ is a monotonically increasing function of M , and its numerical approximation can be found for instance in Kang et al.(2007).

Figure 14 reports the distribution of CR energy flux adopting the KJ02 injection model. The bulk of CR energy injection is achieved for $M \approx 2$, and only a few merging/post-merger clusters show a broader peak of injection up to larger Mach number, $M \sim 4$. The maximum difference can be as high as ~ 100 in the CR energy if relaxing and post-merger systems are compared for $M > 4$ shocks.

Figure 15 presents the radial distribution of mean Mach number, for the volume-weighted average or for the weighting with the thermal and CR energy flux discussed above. The volume-weighted profiles are *extremely flat*, in agreement with previous studies (Vazza, Brunetti & Gheller 2009), with just some strong imprints of internal mergers shocks which increases the average value up to $M \sim 2$ in some post-merger systems. The same is true for the thermal energy weighted profiles, while the profiles become slightly steeper when CR energy flux is the weighting quantity. Interestingly enough, in all cases the occurrence of shocks larger than $M > 2$ within R_v is a rare event, which is qualitatively in agreement with the rare frequency of observed merger shocks in clusters. In particular, from the inspection of Fig.15, we find that only two clusters host strong shocks inside $r_{500} \approx R_v/2$, with

$M \approx 2.7$ (E1) and $M \approx 3.5$ (E2) respectively.

In Fig.16 we computed the projected bolometric X-ray flux ($L_{bol} \sim \rho^2 T^{0.5}$) for the innermost region of the two clusters, and we additionally overlay the maps of CR-energy weighted mean Mach number ($M_{crw,ij} = \langle M_{xy} \cdot f_{CR,xy} \rangle_z / \langle f_{CR,xy} \rangle_z$, where the indices x, y refer to the plane of the image, while the index z runs along the line of sight) for a column of $2Mpc$ along the line of sight. In both cases, the shocks are $\sim 1Mpc$ wide and are located close to r_{500} . It is intriguing that we found only two powerful $M > 2.5$ shocks inside r_{500} within a sample of 20 galaxy clusters. This ratio is roughly similar to the ratio of clearly detected shocks in real clusters, which are presently 3 out of $\sim 30 - 40$ clusters imaged by CHANDRA (e.g. Markevitch & Vikhlinin 2007 and references therein). This is statistically compatible with the view that on average only 1–2 strong shocks cross the inner region of massive galaxy clusters during their lifetime: $t_{life} \sim 5Gyr$ for $M \sim 10^{15}M_{\odot}$ objects, while the crossing time of these strong ($M \sim 2 - 3$) shocks inside r_{500} is of the order of $t_{cross} \sim 2r_{500}/Mc_s \sim 0.5Gyr$, which gives a chance of only $\sim 1/10$ to find a strong shocks crossing r_{500} at a given time of observation.

In the Appendix (B) we present the complete set of projected CR energy flux for all clusters in the sample (showing the estimated contribution from the accelerated particles of $E \approx GeV$), with the overlaid bolometric X-ray luminosity for each cluster (Fig.20). The pattern of projected CR fluxes in merging clusters tend to be very sharp, even if projected across the whole cluster volume.

Finally, we report in Fig.17 the integrated ratio between injected CR energy and thermal flux inside a give radius, for the KJ02 model and also for a more recent model presented by the same authors (Kang & Jones 2007). In this second model, the effect of Alfvén wave drift and dissipation in the shock precursor are accounted in a self consistent way, and this yields a value of $\eta(M)$ which is smaller than that adopted by KJ02, at least for $M < 20$. As a consequence the resulting distribution of the energy flux dissipated in clusters by the acceleration of CR as a function of the shock–Mach number is flatter than that obtained by adopting KJ02, and the volume integrated injection efficiency are significantly reduced (Kang et al.2007).

In both cases the estimated ratio is ~ 5 per cent inside $0.2R_v$, while inside R_v the ratio is ~ 20 per cent for KJ02 and ~ 10 per cent for Kang & Jones (2007). Only one

strong post-merger system shows the presence of a systematically larger ratio, $\sim 20 - 30$ percent inside R_v . These results qualitatively support (with a much improved statistical sample, and with ~ 10 better spatial resolution) the findings of Vazza, Brunetti & Gheller (2009).

4. Discussion and Conclusions

In this paper, we presented a sample of 20 massive galaxy clusters in the range of total masses $6 \cdot 10^{14}M_{\odot} \leq M \leq 2 \cdot 10^{15}M_{\odot}$, extracted from large scale cosmological simulations and re-simulated with high mass resolution for the DM particles and high spatial resolution for the gas component, up to $\sim 2 - 3R_v$ from their centers.

We used the ENZO code with Adaptive Mesh Refinement, using a refinement criterion based on gas/DM overdensity and 1–D jumps in the velocity field (as in Vazza et al.2009).

With this approach, we obtained a statistical sample with unprecedentedly large dynamical range within the virial volume of massive galaxy clusters, which can be used to study in detail the thermal properties, accretion phenomena and chaotic processes in the ICM over 2–3 decades in spatial scale, for each cluster.

We presented the first exploratory statistic study of this sample, showing the properties of gas density, gas temperature, gas entropy and baryon fraction for all clusters in our sample and the radial profiles in the range $0.01 \leq r/R_v \leq 3$ (Sections 3.1-3.2). The reported trends are in line with previous studies that used complementary numerical techniques (e.g. SPH or standard AMR simulations), however they make possible to considerably extend the possibility of performing these measurements at much larger radii, thanks to the high spatial resolution in our simulations.

The additional mesh refinement scheme adopted in this work (based on Vazza et al.2009) is explicitly designed to focus also on shock features and chaotic motions leading to significant 1–D jumps in the velocity field. This allowed us to characterize the morphologies, frequency and energy distributions of shock waves in these massive systems (Sec.3.3 with unprecedented resolution and to estimate their relative efficiency in accelerating Cosmic Rays particles, by adopting two reference model of diffusive shock acceleration (Kang & Jones 2002,07). In agreement with previous studies based on much lower reso-

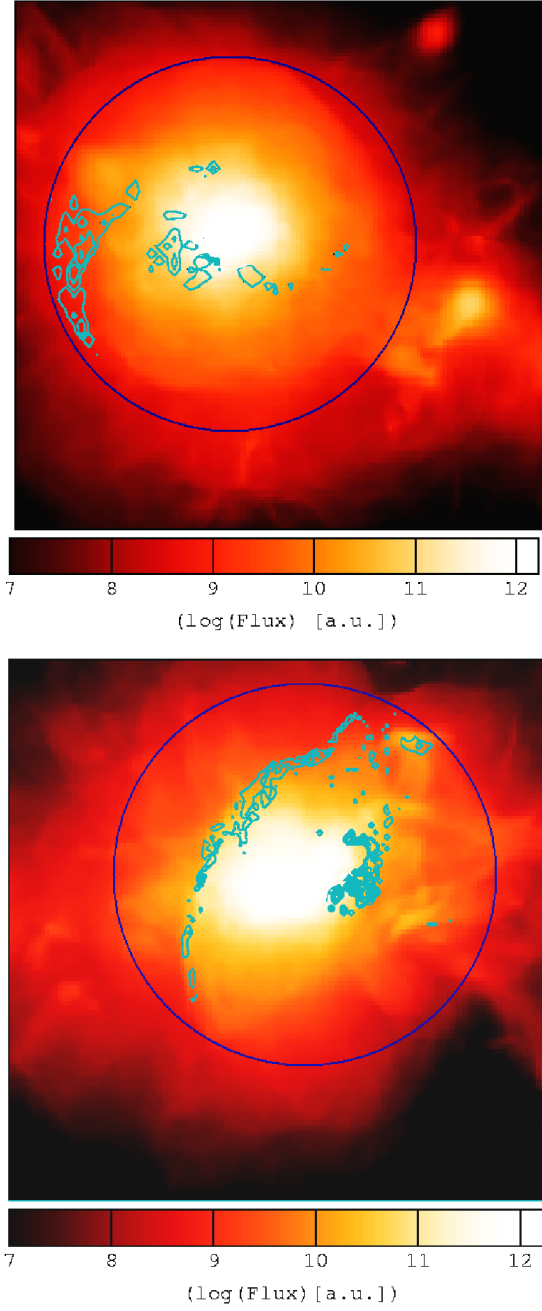


Figure 16: Colors: projected bolometric X-ray emission for clusters E1 and E2 (in arbitrary units); contours: CR-energy weighted maps of Mach number (only shocks with $M_{crw} > 2.5$ are shown) for the same two clusters. The side of both images is $1.7Mpc/h$, the additional blue circles show the approximate location of r_{500} for the two objects.

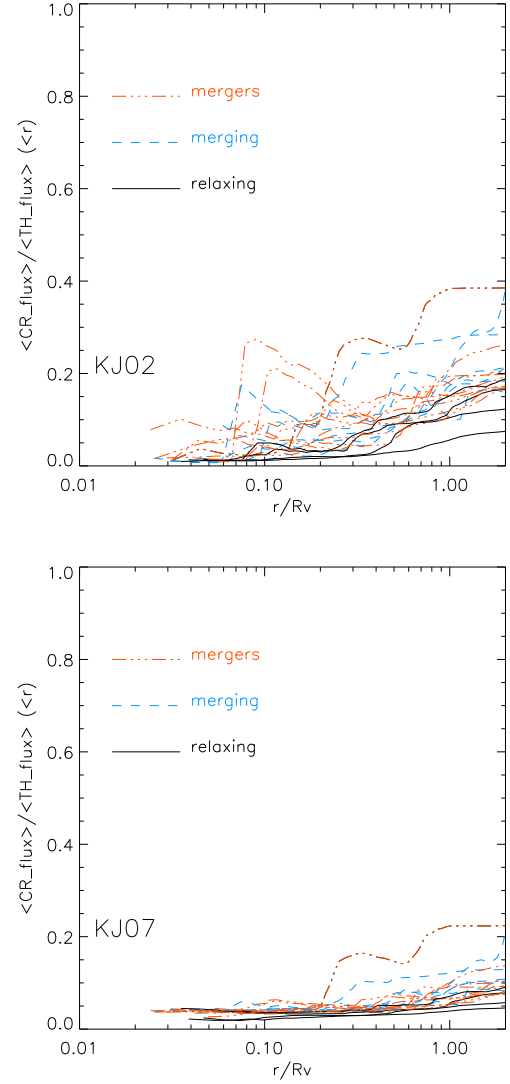


Figure 17: Radial profiles for the integrated ratio between CR-flux and thermal energy flux. The top panel is for the Kang & Jones (2002) injection model, while the bottom panel is for the Kang & Jones (2007) injection model.

lution we confirm that the distribution of shock energy flux inside clusters is extremely steep ($\alpha_{th} \approx -4 \div -5$, with $f_{th}(M)M \propto M^{\alpha_{th}}$), that the peak of the thermalisation at shocks is located at $M \approx 2$, and that the average Mach number inside clusters is small, $M \sim 1.5$.

Only two clusters over 20 are interested by strong shocks inside $R_v/2$ (at $z = 0$), with $M \sim 2.7$ and ~ 3.5 respectively. The rarity of strong shocks found for $r < R_v/2$ is in line with the statistics from X-ray observations of galaxy clusters.

We find that the injection rate of Cosmic Rays is ~ 5 per cent of the thermalized energy within the clusters core, and 10 – 20 per cent inside R_v , with a small dependence on the clusters dynamical state. The behavior of shock surfaces in our simulations can be followed up to large distances thanks to the resolution obtained with our AMR scheme, and potentially allows us to describe with better detail the large scale shocks with respects to precedent studies with SPH simulations (e.g. Pfrommer et al.2007; Hoeft et al.2008) or grid simulations based on standard AMR (e.g. Skillman et al.2008). We find energy flux distributions at shocks that are steeper than those obtained by Pfrommer et al.2007 (with the energies flux reduced by ~ 10 times at $M \sim 10$). The morphologies of the shocks present much sharper features (e.g. edges), even when projected across the cluster volume (see also Appendix B).

At least part of this difference is due to differences in the effective resolution of shock waves inside and outside clusters, which is preserved up to the maximum available resolution by the AMR scheme in our runs (while it can strongly vary in SPH simulations). Also, the differences in the thermal gas distribution at large radii discussed in Sect.3.2 may play a role in giving difference in the properties of the shock waves in the accretion regions simulated by the two approaches.

In conclusion, we have presented a first look at a large sample of massive galaxy clusters simulated with AMR techniques, leading to an unprecedented level of spatial detail up to large distances from the cluster centers. This offers an important possibility to study the thermal and non thermal properties of rich cluster of galaxies with a very large dynamical range in spatial scale, in a fully cosmological framework. A public archive of data has been build and made accessible via web (at the URL: <http://data.cineca.it> under the *IRA-CINECA Simu-*

lated Cluster Archive section), which we encourage to access and use to produce further cluster studies and to complement our results using other approaches.

5. acknowledgments

We acknowledge partial support through grant ASI-INAF I/088/06/0 and PRIN INAF 2007/2008, and the usage of computational resources under the CINECA-INAF 2008-2010 agreement and the 2009 Key Project “Turbulence, shocks and cosmic rays electrons in massive galaxy clusters at high resolution”. We thank S.Etteri for providing the data-points of the baryon fraction in Gadget simulated clusters. We thank A.Adamo, A.Bonafede, S.Cantalupo, R.Cassano, M.Meneghetti, M.Roncarelli and A. Vikhlinin for useful discussions.

References

- [1] Agertz O., et al., 2007, MNRAS, 380, 963
- [2] Aharonian F., et al., 2009, ApJ, 691, 175
- [3] Aleksić, J., et al. 2010, ApJ, 710, 634
- [4] Berger M. J., Colella P., 1989, JCoPh, 82, 64
- [5] Bagchi, J., Durret, F., Neto, G. B. L., & Paul, S. 2006, Science, 314, 791
- [6] Bautz, M. W., et al. 2009, PASJ, 61, 1117
- [7] Berrington, R. C., & Dermer, C. D. 2003, ApJ, 594, 709
- [8] Bonafede, A., et al. 2009, A & A, 503, 707
- [9] Borgani, S., Fabjan, D., Tornatore, L., Schindler, S., Dolag, K., & Diaferio, A. 2008, Space Science Reviews, 134, 379
- [10] Borgani, S., & Kravtsov, A. 2009, arXiv:0906.4370
- [11] Brunetti G., Venturi T., Dallacasa D., Cassano R., Dolag K., Giacintucci S., Setti G., 2007, ApJ, 670, L5
- [12] Bryan G. L., Norman M. L., 1997, ASPC, 123, 363

- [13] Churazov, E., Forman, W., Vikhlinin, A., Tremaine, S., Gerhard, O., & Jones, C. 2008, MNRAS, 388, 1062
- [14] Comparato M., Becciani U., Costa A., Larsson B., Garilli B., Gheller C., Taylor J., 2007, PASP, 119, 898
- [15] Dolag K., Vazza F., Brunetti G., Tormen G., 2005, MNRAS, 364, 753
- [16] Dolag, K., Borgani, S., Schindler, S., Diaferio, A., & Bykov, A. M. 2008, Space Science Reviews, 134, 229
- [17] Donnert, J., Dolag, K., Brunetti, G., Cassano, R., & Bonafede, A. 2010, MNRAS, 401, 47
- [18] Ettori S., Dolag K., Borgani S., Murante G., 2006, MNRAS, 365, 1021
- [19] Fakhouri, O., Ma, C.-P., & Boylan-Kolchin, M. 2010, arXiv:1001.2304
- [20] Frenk, C. S., et al. 1999, ApJ, 525, 554
- [21] Gabici S., Blasi P., 2003, ApJ, 583, 695
- [22] George, M. R., Fabian, A. C., Sanders, J. S., Young, A. J., & Russell, H. R. 2009, MNRAS, 395, 657
- [23] Gheller C., Pantano O., Moscardini L., 1998, MNRAS, 296, 85
- [24] Giacintucci, S., et al. 2008, ApJ, 682, 186
- [25] Godunov, S. K. 1959, Mat. Sbornik, 47, 271
- [26] Haardt F., Madau P., 1996, ApJ, 461, 20
- [27] Hockney, R. W., & Eastwood, J. W. 1981, Computer Simulation Using Particles, New York: McGraw-Hill, 1981,
- [28] Hoeft, M., Brügggen, M., Yepes, G., Gottlöber, S., & Schwobe, A. 2008, MNRAS, 391, 1511
- [29] Hoshino, A., et al. 2010, arXiv:1001.5133
- [30] Hui, L., & Gnedin, N. Y. 1997, MNRAS, 292, 27
- [31] Iapichino L., Niemeyer J. C., 2008, MNRAS, 388, 1089
- [32] Kang H., Jones T. W., 2002, JKAS, 35, 159
- [33] Kang, H., & Jones, T. W. 2007, Astroparticle Physics, 28, 232
- [34] Kang H., Ryu D., Cen R., Ostriker J. P., 2007, ApJ, 669, 729
- [35] Kawaharada, M., et al. 2010, arXiv:1002.4811
- [36] Kravtsov, A. V., Vikhlinin, A., & Nagai, D. 2006, ApJ, 650, 128
- [37] Loken, C., Norman, M. L., Nelson, E., Burns, J., Bryan, G. L., & Motl, P. 2002, ApJ, 579, 571
- [38] Madau, P., & Efstathiou, G. 1999, ApJL, 517, L9
- [39] Maier, A., Iapichino, L., Schmidt, W., & Niemeyer, J. C. 2009, arXiv:0909.1800
- [40] Markevitch, M., Govoni, F., Brunetti, G., & Jerius, D. 2005, ApJ, 627, 733
- [41] Markevitch, M. 2006, The X-ray Universe 2005, 604, 723
- [42] Markevitch, M., & Vikhlinin, A. 2007, Phys.Rev.Ser., 443, 1
- [43] Miniati F., Jones T. W., Kang H., Ryu D., 2001, ApJ, 562, 233
- [44] Mitchell, N. L., McCarthy, I. G., Bower, R. G., Theuns, T., & Crain, R. A. 2009, MNRAS, 395, 180
- [45] Molnar, S. M., Hearn, N., Haiman, Z., Bryan, G., Evrard, A. E., & Lake, G. 2009, ApJ, 696, 1640
- [46] Norman M. L., Bryan G. L., Harkness R., Bordiner J., Reynolds D., O'Shea B., Wagner R., 2007, arXiv, 705, arXiv:0705.1556
- [47] O'Shea, B. W., Nagamine, K., Springel, V., Hernquist, L., & Norman, M. L. 2005, ApJ, 160, 1
- [48] Paul, S., Iapichino, L., Miniati, F., Bagchi, J., & Mannheim, K. 2010, arXiv:1001.1170

- [49] Piffaretti, R., & Valdarnini, R. 2008, *A&A*, 491, 71
- [50] Pfrommer C., Enßlin T. A., Springel V., Jubelgas M., Dolag K., 2007, *MNRAS*, 378, 385
- [51] Pratt, G. W., Croston, J. H., Arnaud, M., Bohringer, H. 2009, *A&A*, 498, 361
- [52] Rasia E., et al., 2006, *MNRAS*, 369, 2013
- [53] Reiprich, T. H., et al. 2009, *A&A*, 501, 899
- [54] Robertson, B. E., Kravtsov, A. V., Gnedin, N. Y., Abel, T., & Rudd, D. H. 2010, *MNRAS*, 401, 2463
- [55] Roncarelli, M., Ettori, S., Dolag, K., Moscardini, L., Borgani, S., & Murante, G. 2006, *MNRAS*, 373, 1339
- [56] Rottgering, H. J. A., Wieringa, M. H., Hunstead, R. W., & Ekers, R. D. 1997, *MNRAS*, 290, 577
- [57] Ryu D., Kang H., Hallman E., Jones T. W., 2003, *ApJ*, 593, 599
- [58] Skillman, S. W., O’Shea, B. W., Hallman, E. J., Burns, J. O., & Norman, M. L. 2008, *ApJ*, 689, 1063
- [59] Solovyeva, L., Anokhin, S., Sauvageot, J. L., Teyssier, R., & Neumann, D. 2007, *A&A*, 476, 63
- [60] Springel V., 2005, *MNRAS*, 364, 1105
- [61] Springel, V. 2009, *MNRAS*, 1655
- [62] Tormen, G., Bouchet, F. R., & White, S. D. M. 1997, *MNRAS*, 286, 865
- [63] Vazza F., Tormen G., Cassano R., Brunetti G., Dolag K., 2006, *MNRAS*, 369, L14
- [64] Vazza, F., Brunetti, G., & Gheller, C. 2009, *MNRAS*, 395, 1333
- [65] Vazza, F., Brunetti, G., Kritsuk, A., Wagner, R., Gheller, C., & Norman, M. 2009, *A&A*, 504, 33
- [66] Vazza, F., Gheller, C., & Brunetti, G. 2010, *A&A*, 513, A32
- [67] Voit, G. M., Kay, S. T., & Bryan, G. L. 2005, *MNRAS*, 364, 909
- [68] Wadsley, J. W., Veeravalli, G., & Couchman, H. M. P. 2008, *MNRAS*, 387, 427
- [69] Woodward P., Colella P., 1984, *JCoPh*, 54, 115
- [70] Younger, J. D., & Bryan, G. L. 2007, *ApJ*, 666, 647
- [71] ZuHone, J. A., Markevitch, M., & Johnson, R. E. 2009, arXiv:0912.0237

A. The reionization model

We implemented in ENZO a run-time scheme to update the thermal energy of cosmic baryons, in order to reproduce with accuracy the effect of the a re-heating background due to stars and AGN activity. This is motivated by the fact that any re-ionization model with a gradual radiation turn-off can be well approximated by a suitably chosen sudden turn-on model (Hui & Gnedin 1997). We adopted as fiducial model the re-ionization background by Haardt & Madau (1996) spectrum supplemented with an X-ray Compton heating background from Madau & Efstathiou (1999). The temperature structures of the re-heated cosmic gas across the whole AMR region cluster is very well reproduced at all cosmic epochs, by imposing a temperature floor of $T_0 = 3 \cdot 10^4 K$ in the redshift range of $2 \leq z \leq 7$. After this epoch, we assume that the re-ionization background vanishes in a sharp transition.

Despite its simplicity (which turns into a less intense usage of memory and computation) compared to the run-time re-ionization model implemented in the public version of ENZO, we find that it works very well for the clusters volume and its surroundings.

In Fig.18 we report tests for the application of our modeling of re-ionization in ENZO (T0), comparing with the standard re-ionization scheme model implemented in the public version of ENZO (HM).

Within the whole AMR region, the difference in the distribution is of the order of ~ 10 per cent at the lowest gas densities; if the radial temperature profile for the two clusters is computed, however, differences are at the percent level for all radii up to $\sim 2R_v$ from the clusters centers. Also the other thermodynamical properties of the clusters

(e.g. gas density, gas entropy, etc) are recovered with a similar accuracy if comparing the two methods.

B. Images of all clusters

The visual inspection of projected maps or slices through simulated clusters may provide additional and complementary information to more quantitative proxies, as those presented in Sec.2.3.

In particular, the close inspection to projected maps taken from different line of sight enhances the probability of finding physically meaningful similarity between simulated objected and real galaxy clusters observed in X-ray (e.g. Sovloyeva et al.2007; Donnert et al.2009).

We encourage the interested readers in closely inspecting the whole sample by using the public archive at <http://data.cineca.it/index.php>, and to report interesting similarities with real galaxy clusters.

The panels in Figures 19 show the projected gas density across the whole AMR region of all clusters simulated in the project (maximum along the line of sight) and slices in gas temperature, taken through the center of mass of the same clusters. The size of all images is rescaled to be $\approx 5R_v$ of every object.

The panels in Fig.20 show the projected X-ray bolometric luminosity for all clusters in the sample (colors), and the energy flux along the line of sight for the Cosmic Rays particles accelerated at shocks (contours) This gives a flavor of the patterns of shock waves associated with most of the injection of CR particles, via Shock Diffusive Acceleration (as in Sec.3.3). The CR particles flux was estimated by assuming a Kang & Jones (2002) injection model at each shocks, and by imposing a power law spectrum dependent on the Mach number, $E(p) \propto p^{-s}$ (where $s = 2(M^2 + 1)/(M^2 - 1)$). Only the flux associated to particles of $E \approx 1\text{GeV}$ is displayed as isocontours (which span about 2 orders of magnitude in flux and are spaced in $\Delta \log(E) = 0.2$). In at least three major merger systems (E1,E11 and E18B) we report the evidence of couples of large scale, arc-shaped regions of intense CR acceleration of size $\sim \text{Mpc}$, which are reminiscent of doubles of radio-relics in real galaxy clusters (e.g. Roettgering et al.1997; Bacghi et al.2005; Bonafede et al.2009).

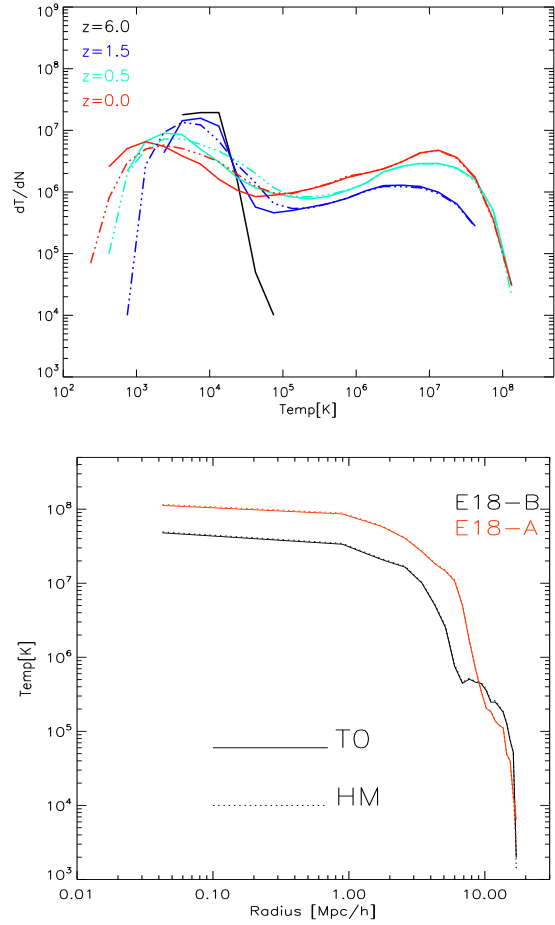


Figure 18: *Top*: temperature distribution functions for the AMR region at 4 redshifts, for the HM re-ionization model (dashed) and for the re-ionization model adopted in the present work (solid), for one of the simulated box of 187Mpc/h. *Bottom*: temperature profiles for the two most massive galaxy clusters formed in the same box as above. The solid lines show the dotted lines show the results for the HM re-ionization model, while the solid lines show the results fro the re-ionization model employed in this work.

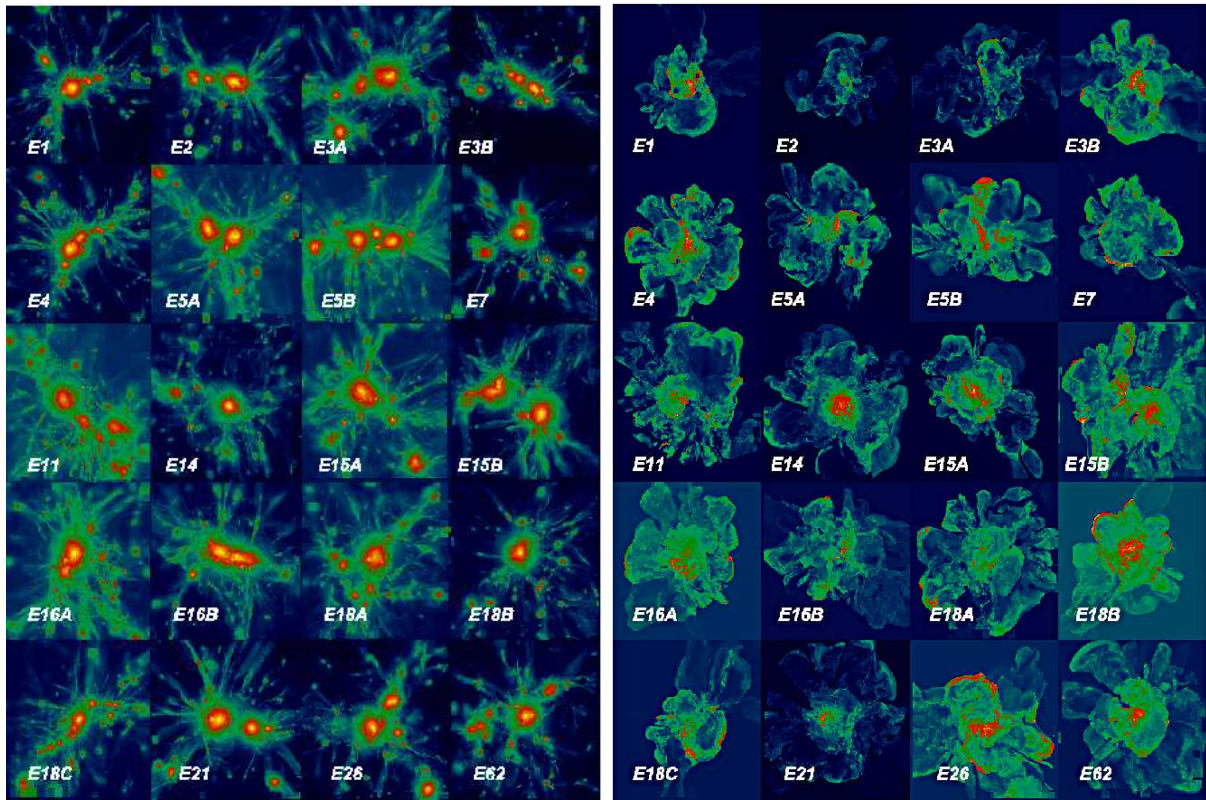


Figure 19: Maximum gas density along the line of sight (left panel) and cut in gas temperature (right panel) for all clusters in the sample. The side of each image is $\approx 5R_v$ of the enclosed galaxy cluster.

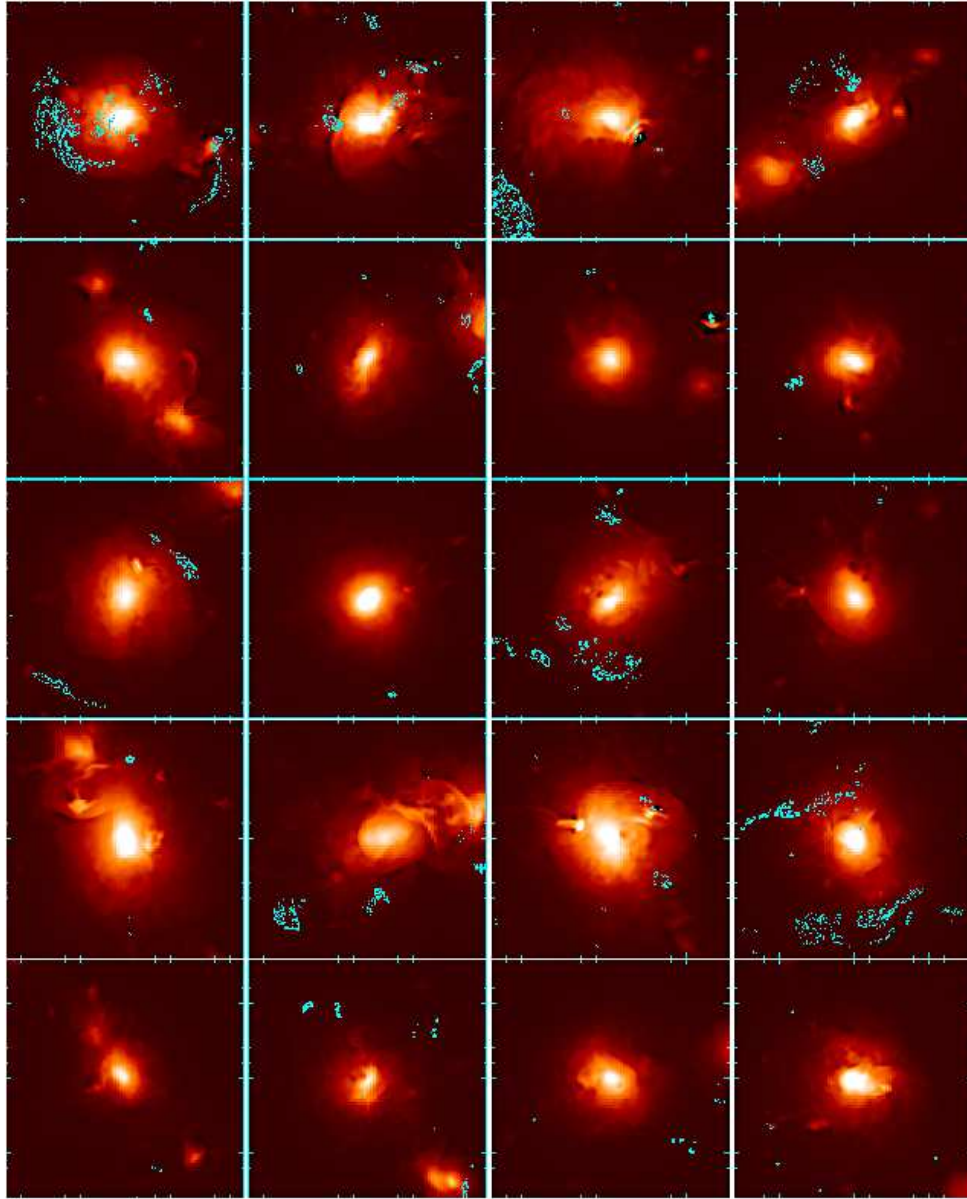


Figure 20: Colors: projected X-ray bolometric luminosity for all clusters in the sample (the color table is as in Fig.16). Contours: energy flux for CR accelerated at shocks, for $E \approx 1 \text{ GeV}$ particles. The contours range for about 2 order of magnitude in flux, and they are spaced by $\Delta \log(E) = 0.2$.